Journal of the Meteorological Society of Japan

The DOI for this manuscript is
DOI:10.2151/jmsj.2024-014
J-STAGE Advance published date: January 17th, 2024
The final manuscript after publication will replace the preliminary version at the above DOI once it is available.

Validation of spaceborne precipitation radar data by rain gauges and disdrometers over the complex topography of the northeastern Indian subcontinent

Fumie MURATA

Faculty of Science and Technology, Kochi University, Kochi, Japan

Toru TERAO

Faculty of Education, Kagawa University, Takamatsu, Japan

Yusuke YAMANE

Faculty of Education, Tokoha University, Shizuoka, Japan

Azusa FUKUSHIMA

Faculty of Humanity, Kobe-Gakuin University, Kobe, Japan

Masashi KIGUCHI

Graduate School of Engineering, the University of Tokyo, Tokyo, Japan

Masahiro TANOUE

Meteorological Research Institute, Tsukuba, Japan

Hideyuki KAMIMERA

National Research Institute for Earth Science and Disaster Resilience, Tsukuba, Japan

Hiambok J. SYIEMLIEH and Laitpharlang CAJEE

Department of Geography, North-Eastern Hill University, Shillong, India

Shamsuddin AHMED and Sayeed Ahmed CHOUDHURY

Bangladesh Meteorological Department, Dhaka, Bangladesh

Prasanta BHATTACHARYA and Abani Kumar BHAGABATI

Department of Geography, Gauhati University, Guwahati, India

Subashisa DUTTA

Indian Institute of Technology Guwahati, Guwahati, India

and

Taiichi HAYASHI

Center for Southeast Asian Studies, Kyoto University, Kyoto, Japan

December 27, 2023

Corresponding author: Fumie Murata, Faculty of Science and Technology, Kochi University, 2-5-1, Akebonocho, Kochi, Kochi 780-8520, Japan.
E-mail: fumie@kochi-u.ac.jp

Abstract

Near-surface rain rate datasets derived from the Tropical Rainfall Measuring Mission Precipitation Radar (TRMM PR) and Global Precipitation Measurement Dual-frequency Precipitation Radar (GPM DPR) and near-surface raindrop size distribution (DSD) parameters derived from the GPM DPR were validated using 43 tipping-bucket rain gauges installed over the northeastern Indian subcontinent and two Parsivel^2 disdrometers installed on the Meghalaya Plateau, India. Both TRMM PR version 7 and version 8 products significantly underestimated the rainfall over the Indian subcontinent during the monsoon season (June–September). The GPM DPR version 06A product also significantly underestimated the rainfall at stations on the Meghalaya Plateau, India. The heavy rainfall area (HRA) of the Meghalaya Plateau in the TRMM PR climatology showed lighter rainfall on the plateau, whereas heavier rainfall was detected in adjacent valleys. Intense surface rainfall over the HRA may be detectable, because such intense rainfalls tended to occur from deeper convections, that were less affected by the ground clutter interferences. A comparison of the statistical features of the DSD parameters between the disdrometers and GPM DPR retrievals around the Meghalaya Plateau confirmed that an adequate assumption of the adjustment factor ϵ is important for improving the DSD parameters in GPM DPR retrievals.

Keywords validation of spaceborne precipitation radar; orographic rainfall; Indian monsoon; raindrop size distribution

1. Introduction

The Tropical Rainfall Measuring Mission (TRMM) and its successor, the Global Precipitation Measurement (GPM), orbit the Earth between 35°S and 35°N and between 65°S and 65°N, respectively. The onboard precipitation radar (TRMM PR) (Kummerow et al. 1998; Kozu et al. 2001; Iguchi et al. 2000, 2009) and dual-frequency precipitation radar (GPM DPR) (Kojima et al. 2012; Hou et al. 2014; Skofronick-Jackson et al. 2017) have provided information on three-dimensional rainfall distributions and aided advanced precipitation research on a global-scale since their launches in 1997 and 2014, respectively (e.g., Houze et al. 2015). These radars have also contributed to global rain rate distribution datasets, such as the Global Satellite Mapping of Precipitation (GSMaP) (Kubota et al. 2020) and Integrated Multi-satellite Retrievals for GPM (IMERG) (Huffman et al. 2020), which use spaceborne microwave sensors with enhanced temporal resolutions. The GPM DPR enables estmations of the mass-weighted mean drop diameter (D_{mass}) of the precipitation drop size distribution (DSD) (Skofronick-Jackson et al. 2017). The normalized gamma DSD (Willis 1984; Testud et al. 2001) and the relationship between rain rate (R) and the D_{mass} were adopted in the GPM DPR algorithm (Seto et al. 2013b). The assumed normalized gamma DSD has two additional parameters: the normalized intercept parameter, N_{w}, and the shape parameter, μ, which has a value equal to 3. The accuracy of the DPR retrieved D_{mass} has been proved to some extent (e.g., D'Adderio et al. 2018; Chase et al. 2020; Gatlin et al. 2020) by a validation with dual-polarization radar data and ground-based disdrometers. Recently, Liao and Meneghini (2022) reported that the range-independent assumption of the adjustable parameter in the R–D_{mass} relation degraded the accuracy of the R and D_{mass} estimation. The spatial distribution of GPM DPR-retrieved D_{mass} values have been described by Radhakrishna et al. (2020) and Yamaji et al. (2020).

Many efforts have been made to validate spaceborne radars that pass over specific locations using data from ground-based rain gauges (e.g., Amitai et al. 2012; Seto et al. 2013b) and ground-based radars (e.g., Wolff et al. 2005; Wolff and Fisher 2008; Amitai et al. 2009; Petracca et al. 2018; Watters et al. 2018; Petersen et al. 2020). Additionally, many methods have been proposed to improve spaceborne radar estimates (e.g., Ma et al. 2020; Arulraj and Barros 2019, 2021; Hirose et al. 2021). Rain gauges are thought to provide the most reliable measurements (Kidd et al. 2017). However, comparative studies of instantaneous TRMM PR near-surface rain rate (NSR) data with in-situ rain gauge networks are limited. One of the reasons for this is the difficulty to obtain rain gauge data with high time resolution; generally, the time resolution of operational rainfall data is coarser than 10 min. In developing countries, this situation is even more severe. For example, the Bangladesh Meteorological Department operationally observes rainfall every 3 h. Therefore, rainfall datasets with high time resolutions are valuable for the validation of spaceborne radar rain retrievals.

The TRMM PR has revealed large spatial gradients of precipitation over complex terrains worldwide (e.g., Nesbitt and Anders 2009; Hirose et al. 2017). However, the estimation of precipitation over complex topography using spaceborne radars contains various errors. For example, ground clutter over the complex terrain raises the clutter free bottom level, making it difficult to detect shallow rain and increasing reflectivity toward the ground, which tends to occur in orographic seeder-feeder clouds (e.g., Prat and Barros 2010; Speirs et al. 2017; Arulraj and Barros 2021; Shimizu et al. 2023). The influence of ground clutter contamination into path-integrated attenuation deteriorates the estimation of near-surface rainfall. In addition, the non-uniform beam filling caused by complex topography results in poor path-integrated attenuation estimates, which are due to the degraded quality of the reference dataset of normalized radar cross section used in the surface reference technique (Meneghini et al. 2015). A better understanding of the characteristics of precipitation over complex terrain is needed to improve the reliability of space-borne radar retrievals.

This study aimed to validate surface rainfall with TRMM PR V7, V8, and GPM DPR V06A products using a tipping-bucket rain gauge network encompassing the northeastern Indian subcontinent based on the method proposed by Terao et al. (2017). The difference in product versions, as well as the difference between instruments used in TRMM PR and GPM Ku-band PR, regulate the performance of precipitation estimation. Furthermore, we attempted to validate the GPM DPR-retrieved DSD parameters using in situ disdrometers located on the Meghalaya Plateau. The study area has a complex topography including the rainfall station "Cherrapunji", which is located on the southern slope of the Meghalaya Plateau and is reported to have the heaviest rainfall in the world (Jennings 1950; Murata et al. 2017). The characteristics are different between premonsoon and monsoon seasons, while diurnal and intraseasonal variations are dominant in this region. Such large spatiotemporal variation in rainfall over the northeastern Indian subcontinent represents a unique testbed to validate rainfall products. The remaining sections of this paper are organized as follows. Section 2 provides details on the datasets and methodology used. The validation results are presented in Section 3, and Section 4 presents the properties of rainfall over the heavy rainfall area (HRA) in Meghalaya. Section 5 discusses the validation of DSD parameters and the contrast in rainfall between the plateau and the valleys over the HRA. Finally, Section 6 provides a summary.

2. Data and analysis method

2.1 Rain gauges

Fig. 1

We installed 43 tipping-bucket type rain gauges manufactured by Ikeda Keiki (Shizuoka, Japan) and Dynalab Weathertech (Maharashtra, India) in Bangladesh and the Assam and Meghalaya Indian states, respectively (Fig. 1). The rain gauges had a resolution of 0.5 mm. Most stations were installed between 2004 and 2006. In 2014, all stations in India were replaced with the same 0.5-mm tipping-bucket rain gauges manufactured by the Komatsu Factory Co., Ltd (Tokyo, Japan). In 2016, we installed four additional rain gauges in Meghalaya. Two were installed in the grid where heavier rainfall was observed by the TRMM PR (see Fig. 2). The analysis period varies depending on the rain gauge site (details are provided in Supplement 1–4). For the data logger, we utilized the HOBO Pendant Event Logger (UA-003-64, Onset Computer Corporation, Bourne, MA, USA). All loggers recorded the timing of tipping with a second resolution. On average, we visited each station once or twice a year to download the accumulated data and adjust the data loggers' clock. However, a maximum clock deviation of several minutes may have still occurred due to logger clock drift.

The rain gauges of our network were matched with spaceborne radar beams whose centers were within the matching radius D according to the procedure adopted by Terao et al. (2017). When multiple beams were obtained, each beam was treated as an independent event, assuming that the information from each satellite footprint was considered as an independent sample for comparison. In the study by Terao et al. (2017) the average of multiple beams was calculated and counted as one event. In the present study, we modified this portion of the method used by Terao et al. (2017) to increase the number of samples. The rain rate from rain gauge data was calculated from the number of tipping within the time window between $t + \tau - \Delta t$ and $t + \tau + \Delta t$. Here, t is the spaceborne radar scanned timing, Δt is the half length of the time window to count tipping, and τ is the estimated time lag during which spaceborne radar-observed precipitation falls and reaches the rain gauge on the ground (Amitai et al. 2012; Seto et al. 2013b; Terao et al. 2017). Terao et al. (2017) examined several sets of these parameters by calculating the correlation coefficient with the spaceborne radar matchups, confirming the best robustness and representativeness for $\tau = 300$ s, $D = 3.5$ km, and $\Delta t = 150$ s.

We applied the percentile method of the bootstrap test (Efron 1979) with a Monte Carlo algorithm to calculate the confidence interval for ensemble averages for the ΔR error. This is the difference between the spaceborne radar NSR of the matched pixel (SAT) and the rain rate of rain gauges during the time window of $2\Delta t$ (RG), expressed as $\Delta R = SAT - RG$. In total, 10,000 resampling averages were calculated for the original observations of ΔR to obtain the 2.5 and 97.5 percentiles, which defined the 95% confidence intervals. This test was performed only when more than 20 non-zero samples were available. Fig. 2

Figure 2 shows the TRMM PR V7 climatological rainfall map over the southern slope of the Meghalaya Plateau based on TRMM PR data from 1998–2013 (Hirose and Okada 2018); elevation contours are also included. The comparison between precipitation distribution and elevation contours revealed that the HRA was distributed over a narrow west-east elongated area, which corresponds to a steep slope area between 500- and 1500-m contours in the southern Meghalaya Plateau. Figure 2 also shows that the rainfall in the HRA is heavier in the valley and lighter on the plateau. However, the rainfall stations renowned for heavy rainfall, Cherrapunji and Mawsynram, and a comparable rainfall station, Pynursla, are located on the plateau. Fig. 3

In May 2017 we installed a new rain gauge at Cherrapunji beside the disdrometer in the India Meteorological Department (IMD) observatory to validate the disdrometer. Figure 3a shows a comparison between the daily rainfall measured by the rain gauge in the IMD observatory and that measured by our rain gauge network in the Cherrapunji station. The IMD observatory is located approximately 1 km east of our Cherrapunji station, closer to the edge of the plateau. Figure 3b compares the daily rainfall measured by the rain gauge at the IMD observatory and that measured by the rain gauge station at Sohkhme, 6 km southeast of the IMD site. The Sohkhme village is located in a valley within the heavier rainfall grid of the TRMM climatological rain map (Fig. 2). We confirmed a high correlation between the neighboring gauges in Figs. 3a and b. The obtained regression coefficients show that rainfall at the IMD site was higher than that measured at Cherrapunji with our rain gauge network and that at Sohkhme. The average rainfall during the simultaneous observation period was higher at the rain gauge located on the plateau than that in the valley. The bootstrap test, which examined the difference in the averages of artificially resampled data, showed that the rainfall deficit between the data collected at Sohkhme and the IMD observatory was nearly statistically significant with a 90% confidence interval. The causes for the observed differences in rainfall between the plateau and valley are discussed in Sections 4.3 and 5.

2.2 Disdrometers

We utilized a second-generation laser optical OTT PARticle SIze and VELocity ($Parsivel^2$) disdrometer (Tokay et al. 2014). This device simultaneously measures the fall speed and size of precipitation particles. The smallest observable diameter was 0.312 mm. We first conducted a quality check of the disdrometer data as follows. First, data with a bad sensor status > 1 were excluded. The periods within and after heavy rainfall sometimes result in bad sensor status or missing data. Kalina et al. (2014) considered three sources of error: strong wind effects, raindrops falling within the margin of the observation area, and splash. Raindrops with a fall speed 60% faster or slower than the empirical fall speed–diameter relationship (Gunn and Kinzer 1949; Atlas et al. 1973) were eliminated to avoid these errors, though the number of eliminated data was small. Finally, DSDs with more than 100 raindrops were used to avoid the distortion associated with the estimation of DSD shapes (Smith and Liu 1993; Smith 2016).

The modeled DSD in normalized gamma form (Willis 1984; Testud et al. 2001; Bringi et al. 2002) has three parameters, namely, N_w, D_mass, and μ. N_w is the normalized intercept parameter and represents the intercept of an equivalent exponential DSD with the same liquid water content and mass-weighted mean diameter D_mass as the gamma DSD (Testud et al. 2001); μ is a shape parameter. Throughout this paper, the main unit of N_w is decibels, which equals $10\log_{10}N_{\rm w}$, while the original unit of $N_{\rm w}$ is $\rm m^{-3}mm^{-1}$. A comparison with a spaceborne radar was conducted using the same rain-rate validation method (Section 2.1). Parameters D, Δt, and τ were assigned values of 3.5 km, 180 s, and 300 s, respectively. The selection of Δt changed from 150 to 180 s because the time resolution of disdrometers was 1 min. Thus, a time window spanning 2–8 min after the passage of the satellite was utilized for the comparison.

The 1 min rain samples were observed using two disdrometers installed in the Cherrapunji IMD (91.734°E, 25.269°N) and on the rooftop of the building of the Department of Geography, North–Eastern Hill University (91.896°E, 25.610°N) in Shillong (Fig. 2) from May 2017 to March 2020. A tipping-bucket rain gauge was installed at each station, and the number of tippings was recorded every 1 min to validate the disdrometer-derived rainfall. We found that the disdrometer systematically underestimated hourly rainfall at Cherrapunji, by approximately 30% (Murata et al. 2020).

2.3 Spaceborne radars

This study primarily employed the TRMM PR V8 data from June 2004 to March 2014 and the GPM DPR V6A from March 2014 to March 2020. Both datasets use the same retrieval algorithms. TRMM PR V7 was used to confirm the effect of a longer analysis period compared with the results of Terao et al. (2017). The dataset for the dual-frequency algorithm (DPR Level-2 product, DPRL2 hereafter) was applied using measurements from either the Ku-band, Ka-band, or both when available (Seto et al. 2013a; Seto and Iguchi 2015; Seto et al. 2021). The DPR algorithm assumes that the DSD follows a normalized gamma form, as described in Section 2.2, where μ is set to 3 and D_{mass} and N_{w} are obtained from GPM DPR observations. The DPRL2 algorithm uses the relationship between rain rate R (mm h^{-1}) and D_{mass} (mm), as presented in the following equations for stratiform and convective rain types, respectively:

$$R = 0.392\epsilon^{4.815} D_{\mathrm{mass}}^{6.131} \qquad \text{for stratiform rain}$$

$$R = 1.348\epsilon^{4.373} D_{\mathrm{mass}}^{5.418} \qquad \text{for convective rain}$$

where ϵ is the adjustment factor. Note that the R–D_{mass} relation used in the GPM DPR V6 is different from both the GPM DPR V5 and V7. The precipitation classification method for spaceborne radars is described by Awaka et al. (2021). Stratiform rain is mainly defined by the detection of bright bands, while convective rain includes not only precipitation with large radar reflectivity but also shallow convections. In the DPRL2 algorithm, the dual-frequency surface reference technique (Meneghini et al. 2015) and radar reflectivity factor of the Ka-band precipitation radar were used to adjust ϵ (Seto et al. 2021). We validated D_{mass} and N_{w} at the clutter-free bottom (CFB) level using ground-based rain gauges and disdrometers. The estimation of the CFB level was different between TRMM PR V7 and V8, and the CFB level in V8 was further raised up when the contamination with the sidelobe clutter occurred.

3. Validation results

3.1 Rainfall

Table 1

Table 2

We compared the rainfall matchups between rain gauge data and the NSR of the TRMM PR V7, TRMM PR V8, and GPM DPR products over Meghalaya, Meghalaya/new, Assam, Sylhet+Barak, and Bengal Plain areas during the monsoon (June–September) (Table 1) and premonsoon (March–May) (Table 2) seasons. The area classifications of the rain gauge station are shown in Fig. 1.

As presented in Table 1, both the TRMM PR V7 and V8 datasets significantly underestimated rainfall with 99% confidence intervals for all four areas during the monsoon season. However, the latter showed relative improvement over Meghalaya and the Sylhet+Barak areas, which are influenced by orographic rainfall. In contrast, the degree of underestimation increased in the plain areas of Assam and Bengal. GPM DPR V6A showed a significant underestimation for only the Meghalaya area; notably, the new stations installed in Meghalaya (Meghalaya/new) showed overestimated rainfall, although the difference was not statistically significant. Table 2 indicated that TRMM PR V7 significantly overestimated rainfall during the premonsoon season in the Assam and Bengal plains, whereas TRMM PR V8 did not have this issue. Seto (2022) compared the precipitation rate estimates between the TRMM PR V8 and GPM Ku-band PR (KuPR) Version 6, confirming that the precipitation rate estimate of the TRMM PR exceeded that of the GPM KuPR counterpart. The authors attributed this to a larger value of the adjustment factor ϵ related to the adjustment of the attenuation correction with GPM KuPR. Furthermore, there were no significant differences in rainfall among the areas during the premonsoon season for the GPM DPR V6A product (Table 2c).

3.2 DSD parameters

Table 3

Table 3 shows contingency tables for rainfall detection between disdrometers at Cherrapunji (Tables 3a–c) and Shillong (Tables 3d–f), and the GPM DPR NSR matchups during all periods (Tables 3a and d), monsoon season (Tables 3b and e), and premonsoon season (Tables 3c and f). The percentage of GPM DPR misdetection was high at Cherrapunji throughout the year, and the probability of detection (POD) (e.g., Kidd et al. 2012) was 53% (Table 3a). Meanwhile, misdetection was high at Shillong, only during the monsoon season, and the POD value was 53% (Table 3e). The misdetection may also be caused by the difference between the representative spatiotemporal scales of the two measurements. This is because the disdrometer continuously measures at the same position, while the GPM DPR measures the instantaneous return signal from the beam coverage area, which is a circle with a 5.2-km diameter at the nadir. The maximum, mean, and median values of the rain rate observed by disdrometers for the DPR misdetection events were 3.93, 0.74, and 0.16 mm h^{-1} at Cherrapunji, and 0.65, 0.15, and 0.08 mm h^{-1} at Shillong, respectively. The result shows the GPM DPR misses light rains. Fig. 4

Figure 4 shows scatter plot comparisons of the DSD parameters between the disdrometers and GPM DPR retrievals for both rainy samples, distinguished as stratiform and convective types according to the GPM DPR algorithm (Awaka et al. 2021). Most samples were stratiform in Shillong, whereas half were convective at Cherrapunji. Colored marks indicate the rain rates of the samples corresponding to the spaceborne radar NSR. Although the relationship between D_{mass} and rain rate is used in the GPM DPR algorithm, it is unclear in Figs. 4a and b implying a contribution of the adjustment factor ϵ in the algorithm. The D_{mass} of convective rain has both small and large values because both deep convections and shallow rains are classified as convective rain. D_{mass} showed better correspondence between disdrometers and GPM DPR retrievals, and the mean absolute error was <0.5 mm; however, several outliers were included, which deteriorate the correlation coefficient. The correlation coefficient of the N_{w} at Cherrapunji (Fig. 4d) was higher than that at Shillong (Fig. 4c), while the GPM DPR retrievals corresponded rather well with the disdrometer counterpart at Cherrapunji. The N_{w} of the GPM DPR retrievals tended to concentrate in the 30–40 dB range (Figs. 4c and d). Fig. 5

Several studies have identified distinct characteristics in the geographic distribution of D_{mass} and its seasonal variation (Yamaji et al. 2020; Radhakrishna et al. 2020). Figure 5 shows the spatial distribution of average D_{mass} and average N_{w} at the CFB level over the Meghalaya Plateau and adjacent areas of the Bengal Plain during premonsoon and monsoon seasons. The fluctuation of D_{mass} values during the premonsoon season was more significant than that during the monsoon season, reflecting its small rainy samples and a higher percentage of convective rain (Hirose and Nakamura 2002; Islam and Uyeda 2008). During the monsoon season, the value of D_{mass} tended to be small on the Meghalaya Plateau and large in the Bengal Plain south of the Meghalaya Plateau (Fig. 5c). Meanwhile, the N_{w} values in the plateau area were larger than those in the plain area, with a high N_{w} distributed over the southern and western slopes of the plateau, including the HRA (Fig. 5d). Fig. 6

The statistical characteristics of the DSD parameters are sometimes represented by D_{mass}–N_{w} diagrams (e.g., Bringi et al. 2009; Dolan et al. 2018; Arulraj and Barros 2019). The D_{mass}–N_{w} diagrams shown in Figs. 6a and d represent GPM DPR retrievals using the sample bins inside the area drawn in Fig. 2a (90°–93°E, 24.5°–26°N), while Figs. 6b and e correspond to the disdrometers at Cherrapunji. Figs. 6c and f represent the data from Shillong. The GPM DPR retrievals show the concentration of samples with a D_{mass} of 1.0–1.5 mm and N_{w} of 30–35 dB (Fig. 6a), with a low quantity of small drops ($D_{\mathrm{mass}} < 1$ mm) are much less. In contrast, the disdrometers show the concentration of samples with $D_{\mathrm{mass}} < 1$ mm and $N_{\mathrm{w}} \geq 45$ dB at Cherrapunji (Fig. 6b) and $D_{\mathrm{mass}} \approx 1.0$ mm and $N_{\mathrm{w}} \approx 35$–40 dB at Shillong (Figs. 6c). The D_{mass}–N_{w} diagram is distinguished by six rain rate categories in Figs. 6d–f. The minimum rain rate was set as 0.2 mm h^{-1}, which approximately corresponds to the minimum detectable rain rate of the DPR (Skofronick-Jackson et al. 2017). There are differences between the GPM DPR retrievals (Fig. 6d) and the disdrometer results (Figs. 6e and f). For example, the GPM DPR (Fig. 6d), with many large drops ($D_{\mathrm{mass}} \approx$ 2–3 mm) retrieved even for the light rain rate category with less than 5 mm h^{-1}. Moreover, the GPM DPR retrieved large N_{w}(> 45 dB) for the heavy rain rate category with more than 50 mm h^{-1}. These features were not observed in the disdrometers (Figs. 6e and f).

Liao et al. (2020) found that the gamma DSD model fits the power law equation $R = a \times N_\mathrm{w} \times D_\mathrm{mass}^b$, where $a = 1.588 \times 10^{-4}$ and $b = 4.706$, independent of the shape factor μ. Figures 6g–i show that the GPM DPR retrievals and the disdrometer data at Cherrapunji and Shillong fit well with the equation, except at both ends of the line. The accuracy of both small and large D_mass ends may be difficult to discuss because both small and large drops are susceptible to errors in the Parsivel disdrometer observation (e.g., Tokay et al. 2013). However, differences were still observed between retrievals and disdrometers. The smallest limit of R/N_w in each rain rate category increased with D_mass with color gradation clearly observed in the disdrometers (Figs. 6h and i), but it was unclear in the retrievals (Fig. 6g). This feature is related to a distinct reduction in the upper limit of N_w and increase in the lower limit of D_mass with an increase in the rain rate category (Figs. 6e and f).

4. Properties of rainfall over the HRA

4.1 General features

Fig. 7

We estimated the contoured frequency by altitude diagram (CFAD) of stratiform and convective radar reflectivity (Fig. 7a and b) from spaceborne radars over the HRA and compared them with the profiles in other mountainous areas around the globe (Anders and Nesbitt 2015). The convective profiles showed deep convections where the 0.05% frequency contour crossed 40 dBZ at an altitude of approximately 9 km. Conversely, the stratiform profiles showed higher reflectivity below the melting level at approximately 4.5 km of altitude with the 0.05% frequency contour crossing 40 dBZ at around 5 km. The composite over the HRA was generally very similar to the "tropical regime" such as the Himalayas, New Guinea, and the Peruvian Andes, whereas the composites of the convective profile included many shallow convections similar to those of the "wet monsoon regime", such as the Western Ghats and Myanmar coast. Fig. 8

The NSR rainfall distribution of a rare heavy rain case during the TRMM PR overpass, with a rain rate of around 150 mm h^{-1} was simultaneously observed by the rain gauges at Mawsynram and Cherrapunji, while approximately 80 mm h^{-1} was observed at Pynurla (Fig. 8). The HRA was positioned near the edge of the TRMM PR pass. Although the rain intensity of TRMM PR did not match the in-situ rain gauges, the distribution included a very intense rainfall area with rain rates exceeding 100 mm h^{-1}. The intense rainfall area was located over a windward steep slope with a narrow west-east elongated shape, similar to the climatological rainfall distribution (Fig. 2).

4.2 Angle-bin dependence

Fig. 9

Hirose et al. (2021) and Seto et al. (2021) showed that precipitation statistics from the spaceborne radars strongly depend on the scanning angle. Figures 9a–c show the average NSR over the HRA using all-angle bins (Fig. 9a), near-nadir bins (Fig. 9b), and off-nadir bins (Fig. 9c) of the TRMM PR V8. Here, near-nadir (off-nadir) data were defined as the angle bin number of 22–28 (1–21 and 29–49), which corresponds to a local zenith angle of $< 2.5°$ ($> 2.5°$). The NSR corresponds to the rain rate at the CFB, so Fig. 9a using TRMM PR V8 may be different from Fig. 2 using TRMM PR V7 because the estimation method of the CFB level has been changed. Nonetheless, the rain rate was more intense in the valley and less intense on the plateau,as also observed in Fig. 2. The contrast became sharp and the rain rate in the valley was strongest at near-nadir bins (Fig. 9b), consistent with the findings of Hirose et al. (2021).

Table 4

Table 4 shows the contingency tables for surface rainfall detection between the near-nadir and off-nadir data for spaceborne radar matchups with rain gauges over the HRA. The POD was 86% (66%) and the false alarm ratio (FAR) was 39% (53%) for the near-nadir (off-nadir) data, respectively, which confirms the higher accuracy of near-nadir data. The FAR tends to be larger than the errors observed for the disdrometer data (Table 3), which is because the minimum rain gauge resolution is 0.5 mm. The average rate of rainfall detected by the rain gauges (the spaceborne radars) was 17.6 mm h^{-1} (11.8 mm h^{-1}) for near-nadir data, and 19.5 mm h^{-1} (8.2 mm h^{-1}) for off-nadir data, respectively, and implying that near-nadir data represents the rainfall amount better than off-nadir data.

The CFB level itself has angle bin dependence (Hirose et al. 2021). Figures 9d–f show the horizontal distributions of CFB thickness, which corresponds to the distance between the ground and CFB level, for all-angle bins (Fig. 9d), near-nadir bins (Fig. 9e), and off-nadir bins (Fig. 9f). The CFB thickness is large over the steep slope area, with a maximum average value of approximately 1.7 km. The CFB thickness generally decreased in near-nadir bins (Fig. 9e) and increased in off-nadir bins (Fig. 9f), although the degree of change in CFB thickness was rather small in the steep slope area. The CFB thickness of near-nadir bins decreased to less than 1.0 km over the Bengal Plain and on the Meghalaya Plateau; however, it was 1.5 km over the steep slope area.

4.3 Difference in rainfall between plateau and valley

Fig. 10

The 0.05°×0.05° grid on the plateau where Cherrapunji is located was labeled grid-A, while that in the valley where Sohkhme is located was labeled grid-B (Fig. 9a). Figures 10a and b show the rain rate profiles for near-nadir bins in grid-A and grid-B, respectively. Only near-nadir data was used because the performance of the retrievals was better than that for the off-nadir data (Table 4). The red-colored portion represents the profiles between the ground and CFB level. The rain rate below the CFB level are blind owing to ground clutter, so they were retrieved by regarding radar reflectivity as the same at that in the CFB level. The slight decrease in rainfall intensity was a result of considering the denser air near the ground and the slow fall speed rate of raindrops. The ground level and CFB thickness in grid-A are rather uniform, while various ground levels from near sea level to plateau level and CFB thickness of more than 1.5 km are observed in grid-B. A greater number of heavy NSRs with more than 10 mm h^{-1} was observed in grid-B, but most of the NSRs in both grid-A and grid-B were less than 10 mm h^{-1}. Interestingly, heavy NSRs tended to have higher rain rates up to higher altitudes far above the maximum altitude of the plateau. Notably, some heavy NSRs in grid-B were more intense and rapidly increased downward toward the ground. Figure 10c shows the average rain rate profiles for grid-A (black line) and B (blue line). The average rain rate of grid-B was larger than that of grid-A below an altitude of 6 km. The profile of grid-A was nearly constant below 5 km, whereas that of grid-B increases downward, and the rain rate doubled at the 2 km level.

Hamada and Takayabu (2014) reported the presence of suspicious extreme rainfall in the TRMM PR V7 product, mostly over the land. They showed that most suspicious extremes have a significant monotonic increase in radar reflectivity toward the echo bottom and isolated extreme NSR with large differences from the surrounding pixels. Some profiles in grid-B (Fig. 10b) show similar characteristics to the suspicious extreme rainfall. However, they were not removed using the filter proposed by Hamada and Takayabu (2014). Only one of the profiles had the ratio of the NSR to the average NSRs in the four surrounding pixels exceeding 300, but the vertical gradient of the two lowest bins was smaller than 20 dB km^{-1}. Fig. 11

Figure 11 shows 76 vertical profiles of radar reflectivity within the HRA at pixels that matched rain gauges observed more than 30 mm h^{-1}. If the Z–R relationship (Z [mm^6 m^{-3}]=124$\times R$ [mm h^{-1}]$^{1.50}$) is adopted based on the disdrometer observation at Cherrapunji during May–October 2017 (Murata et al. 2020), then 30 mm h^{-1} corresponds to 43 dBZ. Most profiles increased toward the ground below the melting layer, suggesting the dominance of the collisional growth of rain drops or the seeder-feeder process. In addition, the storm-top height (STH) was below 10 km in altitude for the 86% cases, confirming that heavy rain does not necessarily have a tall STH (Hamada et al. 2015). However, intense rain rate cases of more than 80 mm h^{-1} have a comparably higher STH ($\geq$ 8 km) and stronger radar reflectivity throughout the profile ($\geq$ 45 dBZ below the melting layer), confirming that the heavy NSR tends to have higher rain rates extending to higher altitudes

(Fig. 10).

5. Discussion

Here, we discuss the validation of GPM DPR-retrieved DSD parameters with two disdrometers in the Meghalaya Plateau. We also discuss the distinct contrast in TRMM PR climatology over the HRA, which features heavier rainfall in the valley and lighter rainfall on the ridge.

The average values of the spaceborne radar during the monsoon season (Fig. 5) tended to have a relatively smaller D_{mass} and larger N_{w} over the Meghalaya Plateau than those over the plain area in the southern plateau. This is reasonable because the disdrometers exhibited many samples with small D_{mass} and large N_{w} (Fig. 6). This result is also consistent with the characteristics of DSD in orographic rains (e.g., Rosenfeld and Ulbrich 2003). However, samples with small $D_{\mathrm{mass}} < 1$ mm and large $N_{\mathrm{w}} > 45$ dB were rare in the GPM DPR retrievals (Figs. 6a and b). The satellite-retrieved D_{mass} and N_{w} were concentrated in the 1.0–1.5 mm and 30–40 dB ranges, respectively. Gatlin et al. (2020) also reported a severely limited range of N_{w} estimates at approximately 35 dB.

Both GPM DPR retrievals and disdrometers fit well along the line proposed by Liao et al. (2020), implying strong constraints among D_{mass}, N_{w}, and rain rate. Although the relationship between D_{mass} and rain rate is utilized as the basis of the DSD parameter retrievals (Seto et al. 2021), the correlation between D_{mass} and rain rate was weak in Fig. 5, possibly because an adjustment factor ϵ substantially decides the D_{mass} value. Some outliers in Figs. 5a and b show large D_{mass} (≈ 2 mm) for weak rain rate (< 5 mm h^{-1}), while the disdrometer observations (Figs. 6b–c, e–f) feature these outlier values substantially less.

The disdrometer results (Figs. 6h and i) showed that the lower limits of D_{mass} and R/N_{w} increase with R, where R is the rain rate. This indicates that the minimum value of D_{mass} (the maximum value of N_{w} increasing (decreasing) with the rain rate is a principal characteristics of the disdrometer results (Figs. 6e and f), which coincides with other observation results (e.g., Fig. 5 of Tokay et al. 2020). The color gradation in the GPM DPR retrievals was unclear (Figs. 6d and g) and corresponded to the upper-right portion of Fig. 6d, which shows where no data was found in the disdrometer results (Figs. 6e and f). Updating the DSD database in GPM DPR V7 and changing the algorithm from a range-independent ϵ assumption in this validated GPM DPR V6 dataset to a range-variable ϵ model in GPM DPR V7 (Liao and Meneghini 2022) may improve the DSD parameters of the GPM DPR retrievals.

A comparison of the rain rate profiles of near-nadir data between the grid in the valley and that on the plateau (Fig. 10) revealed an intense surface rain rate more frequently in the valley (grid-B). Some intense rain rate profiles and the average profiles in grid-B still imply a possibility of ground clutter contamination in the valley profiles. The high CFB in the valley becomes an obstacle in detecting shallow precipitation in the blind zone below the CFB level (Shimizu et al. 2023). However, the intense NSR profiles tended to have different properties from those of weak profiles in that they have stronger reflectivity up to far above the ground level (Figs. 10 and 11). This suggests that intense NSRs have less influence on the blind zones, implying that the rainfall distribution over the HRA with heavier rainfall in the valley may not be artificial. However, there are still other factors that cause errors in precipitation retrievals from spaceborne radars. For example, the surface backscattering cross-section of spaceborne radars over land also increases in the presence of precipitation, degrading precipitation retrievals by estimating the path-integrated attenuation in the surface reference technique procedure (Seto et al. 2022). Figure 3a showed the daily rainfall at the IMD observatory in Cherrapunji was systematically heavier than that at our Cherrapunji station, which was located further apart from the valley. It also implies that heavier rainfalls are produced in valleys. The newly installed rain gauges in 2016 in the valley (Fig. 3b and Meghalaya/new in Tables 1 and 2) showed rather lower rainfall in the valley. This suggests that there may be differences in rainfall in the valley between rain at the CFB level and that on the ground owing to the effects of environmental fields, such as wind. Further research is necessary to derive stronger conclusions.

The TRMM LIS analysis showed that the frequency of thunder is very severe over the southern Meghalaya Plateau (Dewan et al. 2018), which supports the frequent occurrence of deep convection over the area. Ahmed et al. (2022) conducted numerical modeling to simulate a heavy rainfall case at Mawsynram and produced deep convection that strengthened over the upslope region of the Meghalaya Plateau. The increased horizontal resolution in the simulation led to steeper slopes, which resulted in heavier precipitation in the upslope region. Medina et al. (2003) analyzed intensive observations over the Southern Alps and showed the formation of graupels over the steep slope of the Alps.

6. Summary

In this study, we attempted to validate the rain rate retrieved from TRMM PR V7 and V8 and GPM DPR V6A, and DSD parameters retrieved from GPM DPR V6A with tipping-bucket rain gauges over the northeastern Indian subcontinent and disdrometers installed in the Meghalaya Plateau. We also discussed the features in TRMM PR climatological rainfall distribution that show lighter rainfall on the plateau and heavier rainfall in the adjacent valleys.

The extension of the analysis period of validation based on Terao et al. (2017) supported the underestimation of monsoon precipitation over the northeastern Indian subcontinent and a significant overestimation of pre-monsoon precipitation over the Assam and Bengal plains by TRMM PR V7. A significant underestimation of monsoon precipitation was also observed in the TRMM PR V8; however, a significant underestimation of monsoon precipitation was observed only over Meghalaya in the GPM DPR V6A data.

The statistical features of D_{mass} and N_{w} derived from the disdrometers at Cherrapunji and Shillong were compared with those of the GPM DPR-retrieved D_{mass} and N_{w} around the Meghalaya Plateau. Both disdrometers showed a dominance of rainfall with a large N_{w} and small D_{mass}, which is a feature of orographic rainfall, while the GPM DPR retrieved D_{mass} and N_{w} showed a limited range of variation in comparison. The disdrometer observation fitted well the line proposed by Liao et al. (2020), which is the same as the GPM DPR-retrievals, implying a strong constraint among D_{mass}, N_{w}, and rain rate. The disdrometer results showed that the minimum value of D_{mass} (the maximum value of N_{w}) increases (decreases) with rain rate. As the relationship between D_{mass} and rain rate is used in the retrieval algorithm, the adequate range of adjustment factor ϵ in the relationship is important for improving DSD parameter retrievals. Better assumptions of DSD parameters in the GPM DPR algorithm will greatly develop the understanding of precipitation over the world, because the characteristics of DSD reflect differences in precipitation mechanisms.

TRMM PR climatological rainfall distributions in the monsoon season showed a distinct dependence on topography over the HRA in Meghalaya, with higher rainfall in the valley and lower rainfall on the ridge. Rainfall over complex terrains has various factors that deteriorate the quality of spaceborne radar rain retrieval. This study suggests that the heavy rain over the HRA tended to occur owing to deeper convections and may be less affected by ground clutter blind zones. Such heavy rains were more frequent in the valley than on the plateau. Further observations (e.g., via in-situ weather radars and more detailed analyses) are required to generate conclusions regarding the mechanisms underlying heavy rainfalls over the Meghalaya Plateau. The improved schemes and new parameters in the DPR Version 7 algorithm are also expected to contribute in elucidating a more accurate rainfall distribution. In addition, the achieved enhanced understanding of precipitation characteristics in various meteorological and geographical conditions will be useful to improve satellite-borne precipitation radar retrievals.

Data Availability Statements

The datasets generated and/or analyzed in this study are available from the corresponding author on reasonable request, subject to all authors' permission.

Supplement

Supplements 1–4 show details of rain gauge stations used for the validation with TRMM PR in Meghalaya and Assam areas, and in Sylhet+Barak and Bengal Plain, respectively. Supplements 3 and 4 show details of rain gauge stations used for the validation with GPM DPR in Meghalaya and Assam areas, and in Sylhet+barak and Bengal Plain, respectively.

Acknowledgements

This study was supported by the Japan Aerospace Exploration Agency (JAXA) 8th GPM/TRMM Research Announcements, the JAXA 2nd Research Announcement on Earth Observations, and JSPS KAKENHI Grant Numbers 11691151, 12740269, 1274020, 15651103, 17255002, 18256005, 21403005, 23241057, 23240122, 26220202, 18KK0098, 20H02252, 20H01523, 20H01387, and 22H01298. This study was also partially supported by the Ministry of Education, Culture, Sports, Science and Technology (MEXT) 21st Century COE Program of Kyoto University, "Elucidation of the Active Geosphere from Asia and Oceania to the World", the Japan-Bangladesh joint study project on floods by the Japan International Cooperation Agency (JICA) of MEXT, the grant program for environmental research projects of the Sumitomo Foundation, the collaborative research programs of the Hydrosphere Atmospheric Research Center (Nagoya University), the Institute for Space-Earth Environmental Research (Nagoya University), the Center for Environmental Remote Sensing (Chiba University), the Disaster Prevention Research Institute (Kyoto University), the Research Institute for a Sustainable Humanosphere (Kyoto University), the Research Institude for Applied Mechanics (Kyushu University), Kagawa University and Kochi University. We greatly appreciate those in India and Bangladesh who supported our observational activities in the northeastern Indian subcontinent. The authors thank Dr. A. Hamada and anonymous reviewers for many constructive comments that greatly improved this manuscript.

References

Ahmed, T., J. Lee, H.-G. Jin, and J.-J. Baik, 2022: Processes associated with extremely heavy precipitation in the meghalaya plateau region: a case modelling study. *Quart. J. Roy. Meteor. Soc.*, **148**, 1057–1074.

Amitai, E., X. Llort, and D. Sempere-Torres, 2009: Comparison of TRMM radar rainfall estimates with NOAA next-generation QPE. *J. Meteor. Soc. Japan*, **87(A)**, 109–118.

Amitai, E., C. L. Unkrich, D. C. Goodrich, E. Habib, and B. Thill, 2012: Assessing satellite-based rainfall estimates in semiarid watersheds using the USDA-ARS Walnut Gulch gauge network and TRMM PR. *J. Hydrometeor.*, **13**, 1579–1588.

Anders, A. M., and S. W. Nesbitt, 2015: Altitudinal precipitation gradients in the tropics from Tropical Rainfall Measuring Mission (TRMM) precipitation radar. *J. Hydrometeor.*, **16**, 441–448.

Arulraj, M., and A. P. Barros, 2019: Improving quantitative precipitation estimates in mountainous regions by modelling low-level seeder-feeder interactions constrained by Global Precipitation Measurement dual-frequency precipitation radar. *Remote Sensing of Environment*, **231**, 111213.

Arulraj, M., and A. P. Barros, 2021: Automatic detection and classification of low-level orographic precipitation processes from space-borne radars using machine learning. *Remote Sensing of Environment*, **257**, 112355.

Atlas, D., R. C. Srivastava, and R. S. Sekhon, 1973: Doppler radadr characteristics of precipitation at vertical incidence. *Rev. Geophys.*, **11**, 1–35.

Awaka, J., M. LE, S. Brodzik, T. Kubota, T. Masaki, V. Chandrasekar, and T. Iguchi, 2021: Development of precipitation type classification algorithms for a full scan mode of GPM dual-frequency precipitation radar. *J. Meteor. Soc. Japan*, **99**, 1253–1270.

Bringi, V. N., G.-J. Huang, V. Chandrasekar, and E. Gorgucci, 2002: A methodology for estimating the parameters of a gamma raindrop size distribution model from polarimetric radar data: application to a squall-line event from the TRMM/Brazil campaign. *J. Atmos. Oceanic Technol.*, **19**, 633–645.

Bringi, V. N., C. R. Williams, M. Thurai, and P. T. May, 2009: Using dual-polarized radar and dual-frequency profiler for DSD characterization: a case study from Darwin, Australia. *J. Atmos. Oceanic Technol.*, **26**, 2107–2122.

Chase, R. J., S. W. Nesbitt, and G. M. McFarquhar, 2020: Evaluation of the microphysical assumptions within GPM-DPR using ground-based observations of rain and snow. *Atmosphere*, **11**, 619.

D'Adderio, L. P., G. Vulpiani, F. Porcu, A. Tokay, and R. Meneghini, 2018:

Comparison of GPM core observatory and ground-based radar retrieval of mass-weighted mean raindrop diameter at midlatitude. *J. Hydrometeor.*, **19**, 1583–1598.

Dewan, A., E. T. Ongee, M. M. Rahman, R. Mahmood, and Y. Yamane, 2018: Spatial and temporal analysis of a 17-year lightning climatology over Bangladesh with LIS data. *Theor. Appl. Climatol*, **134**, 347–362.

Dolan, B., B. Fuchs, S. A. Rutledge, and E. A. Barnes, 2018: Primary modes of global drop size distributions. *J. Atmos. Sci.*, **75**, 1453–1476.

Efron, B., 1979: Bootstrap methods: another look at the jackknife. *Ann. Statist.*, **7**, 1–26.

Gatlin, P. N., W. A. Petersen, J. L. Pippitt, T. A. Berendes, D. B. Wolff, and A. Tokay, 2020: The GPM validation network and evaluation of satellite-based retrievals of the rain drop size distribution. *Atmosphere*, **11**, 1010.

Gunn, R., and G. D. Kinzer, 1949: The terminal velocity of fall for water droplets in stagnant air. *J. Meteor.*, **6**, 243–248.

Hamada, A., and Y. N. Takayabu, 2014: A removal filter for suspicious extreme rainfall profiles in TRMM PR 2A25 Version-7 data. *J. Appl. Meteor. Climatol.*, **53**, 1252–1271.

Hamada, A., Y. N. Takayabu, C. Liu, and E. J. Zipser, 2015: Weak linkage between the heaviest rainfall and tallest storms. *Nature Comm.*, **6**, 6213.

Hirose, M., and K. Nakamura, 2002: Spatial and seasonal variation of rain profiles over Asia observed by spaceborne precipitation radar. *J. Climate*, **15**, 3443–3458.

Hirose, M., and K. Okada, 2018: A 0.01° resolving TRMM PR precipitation climatology. *J. Appl. Meteor. Climatol.*, **57**, 1645–1661.

Hirose, M., S. Shige, T. Kubota, F. A. Furuzawa, H. Minda, and H. Masunaga, 2021: Refinement of surface precipitation estimates for the dual-frequency precipitation radar on the GPM core observatory using near-nadir measurements. *J. Meteor. Soc. Japan*, **99**, 1231–1252.

Hirose, M., Y. N. Takayabu, A. Hamada, S. Shige, and M. K. Yamamoto, 2017: Spatial contrast of geographically induced rainfall observed by TRMM PR. *J. Climate*, **30**, 4165–4184.

Hou, A. Y., R. K. Kakar, S. Neeck, A. A. Azarbarzin, C. D. Kummerow, K. Kojima, R. Oki, K. Nakamura, and T. Iguchi, 2014: The global precipitation measurement mission. *Bull. Amer. Meteor. Soc.*, **95**, 701–722.

Houze, R. A. J., K. L. Rasmussen, M. D. Zuluaga, and S. R. Brodzik, 2015: The variable nature of convection in the tropics and subtropics: a legacy of 16 years of the tropical rainfall measuring mission satellite. *Rev. Geophys.*, **53**, 994–1021.

Huffman, G. J., D. T. Bolvin, D. Braithwaite, K.-L. Hsu, R. J. Joyce, C. Kidd, E. J. Nelkin, S. Sorooshian, E. F. Stocker, J. Tan, D. B. Wolff, and P. Xie, 2020: Integrated Multi-satellite Retrievals for the Global Precipitation Measurement (GPM) mission (IMERG). in: Levizzani V., Kidd C., Kirschbaum D., Kummerow C., Nakamura K., Turk F. (eds) satellite precipitation measurement. *Advances in Global Change Research*, **67**, 445–457.

Iguchi, T., T. Kozu, J. Kwiatkowski, R. Meneghini, J. Awaka, and K. Okamoto, 2009: Uncertainties in the rain profiling algorithm for the TRMM precipitation radar. *J. Meteor. Soc. Japan*, **87A**, 1–30.

Iguchi, T., T. Kozu, R. Meneghini, J. Awaka, and K. Okamoto, 2000: Rain-profiling algorithm for the TRMM precipitation radar. *J. Appl. Meteor. Climatol.*, **39**, 2038–2052.

Islam, M. N., and H. Uyeda, 2008: Vertical variations of rain intensity in different rainy periods in and around Bangladesh. *Int. J. Climatol.*, **28**, 273–279.

Jennings, A. H., 1950: World's greatest observed point rainfalls. *Mon. Wea. Rev.*, **78**, 4–5.

Kalina, E. A., K. Friedrich, S. M. Ellis, and D. W. Burgess, 2014: Comparison of disdrometer and X-band mobile radar observations in convective precipitation. *Mon. Wea. Rev.*, **142**, 2414–2435.

Kidd, C., P. Bauer, J. Turk, G. J. Huffman, R. Joyce, K. L. Hsu, and D. Braithwaite, 2012: Intercomparison of high-resolution precipitation products over northwest Europe. *J. Hydrometeor.*, **13**, 67–83.

Kidd, C., A. Becker, G. J. Huffman, C. L. Muller, P. Joe, G. Skofronick-Jackson, and D. B. Kirschbaum, 2017: So, how much of the earth's surface's covered by rain gauges? *Bull. Amer. Meteor. Soc.*, **98(1)**, 69–78.

Kojima, M., T. Miura, K. Furukawa, Y. Hyakusoku, T. Ishikiri, H. Kai, T. Iguchi, H. Hanado, and K. Nakagawa, 2012: Dual-frequency precipitation radar (DPR) development on the global precipitation measurement (GPM) core observatory. *Proc. SPIE 8528, Earth Observ-*

ing Missions and Sensors: Development, Implementation, and Characterization, **2**, 85281A.

Kozu, T., T. Kawanishi, H. Kuroiwa, M. Kojima, K. Oikawa, H. Kumagai, K. Okamoto, M. Okumura, H. Nakatsuka, and K. Nishikawa, 2001: Development of precipitation radar onboard the Tropical rainfall measuring mission (TRMM) satellite. *IEEE Transactions on Geoscience and Remote Sensing*, **39(1)**, 102–116.

Kubota, T., K. Aonashi, T. U. S. Shige, Y. N. Takayabu, M. Kachi, Y. Arai, T. Tashima, T. Masaki, N. Kawamoto, T. Mega, M. K. Yamamoto, A. Hamada, M. Yamaji, G. Liu, and R. Oki, 2020: Global satellite mapping of precipitation (GSMaP) products in the GPM era. in: Levizzani V., Kidd C., Kirschbaum D., Kummerow C., Nakamura K., Turk F. (eds) satellite precipitation measurement. *Advances in Global Change Research*, **67**, 458–477.

Kummerow, C., W. Barnes, T. Kozu, J. Shiue, and J. Simpson, 1998: The tropical rainfall measuring mission (TRMM) sensor package. *J. Atmos. Oceanic Technol.*, **15**, 809–817.

Liao, L., and R. Meneghini, 2022: GPM DPR retrievals: algorithm, evaluation, and validation. *Remote Sensing*, **14**, 843.

Liao, L., R. Meneghini, T. Iguchi, and A. Tokay, 2020: Characteristics of DSD bulk parameters: implication for radar rain retrieval. *Atmosphere*, **11**, 670.

Ma, Y., V. Chandrasekar, and S. K. Biswas, 2020: A bayesian correction approach for improving dual-frequency precipitation radar rainfall rate estimates. *J. Meteor. Soc. Japan*, **98(3)**, 511–525.

Medina, S., and R. A. J. Houze, 2003: Air motions and precipitation growth in Alpine storms. *Quart. J. Roy. Meteor. Soc.*, **129**, 345–371.

Meneghini, R., H. Kim, L. Liao, J. A. Jones, and J. M. Kwiatkowski, 2015: An initial assessment of the surface reference technique applied to data from the dual-frequency precipitation radar (DPR) on the GPM satellite. *J. Atmos. Oceanic Technol.*, **32**, 2281–2296.

Murata, F., T. Terao, K. Chakravarty, H. J. Syiemlieh, and L. Cajee, 2020: Characteristics of orographic rain drop-size distribution at Cherrapunji, northeast India. *Atmosphere*, **11**, 777.

Murata, F., T. Terao, H. Fujinami, T. Hayashi, H. Asada, J. Matsumoto, and H. J. Syiemlieh, 2017: Dominant synoptic disturbance in the extreme rainfall at cherrapunji, northeast India, based on 104 years of rainfall data (1902-2005). *J. Climate*, **30**, 8237–8251.

Nesbitt, S. W., and A. M. Anders, 2009: Very high resolution precipitation climatologies from the Tropical Rainfall Measuring Mission Precipitation Radar. *Geophys. Res. Lett.*, **36**, L15815.

Petersen, W. A., P. E. Kirstetter, J. Wang, D. B. Wolff, and A. Tokay, 2020: The GPM ground validation program. in: Levizzani V., Kidd C., Kirschbaum D., Kummerow C., Nakamura K., Turk F. (eds) satellite precipitation measurement. *Advances in Global Change Research*, **67**, 471–502.

Petracca, M., L. P. D. Adderio, F. Porcu, G. Vulpiani, S. Sebastianelli, and S. Puca, 2018: Validation of GPM dual-frequency precipitation radar (DPR) rainfall products over Italy. *J. Hydrometeor.*, **19**, 907–925.

Prat, O. P., and A. P. Barros, 2010: Assessing satellite-based precipitation estimates in the Southern Appalachian mountains using rain gauges and TRMM PR. *Adv. Geosci.*, **25**, 143–153.

Radhakrishna, B., K. Saikranthi, and T. N. Rao, 2020: Regional differences in raindrop size distribution wihin Indian subcontinent and adjoining seas as inferred from Global Precipitation Measurement Dual-frequency Precipitation Radar. *J. Meteor. Soc. Japan*, **98(3)**, 573–584.

Rosenfeld, D., and C. W. Ulbrich, 2003: Cloud microphysical properties, processes, and rainfall estimation opportunities. *Meteor. Monogr.*, **52**, 237–258.

Seto, S., 2022: Examining the consistency of precipitation rate estimates between the TRMM and GPM Ku-band radars. *SOLA*, **18**, 53–57.

Seto, S., and T. Iguchi, 2015: Intercomparison of attenuation correction methods for the GPM dual-frequency precipitation radar. *J. Atmos. Oceanic Technol.*, **32**, 915–926.

Seto, S., T. Iguchi, and R. Meneghini, 2022: Correction of path-integrated attenuation estimates considering the soil moisture effect for the GPM dual-frequency precipitation radar. *J. Atmos. Oceanic Technol.*, **39**, 803–821.

Seto, S., T. Iguchi, R. Meneghini, J. Awaka, T. Kubota, T. Masaki, and N. Takahashi, 2021: The precipitation rate retrieval algorithms. *J. Meteor. Soc. Japan*, **99(2)**, 205–237.

Seto, S., T. Iguchi, and T. Oki, 2013a: The basic performance of a precipitation retrieval algorithm for the Global Precipitation Measurement mission's single/dual-frequency radar measurements. *IEEE Trans. Geosci. Remote Sens.*, **51**, 5239–5251.

Seto, S., T. Iguchi, N. Utsumi, M. Kiguchi, and T. Oki, 2013b: Evaluation of extreme rain estimates in the TRMM/PR standard product version 7 using high-temporal-resolution rain gauges datasets over japan. *SOLA*, **9**, 98–101.

Shimizu, R., S. Shige, T. Iguchi, C.-K. Yu, and L.-W. Cheng, 2023: Narrowing the blind zone of the GPM dual-frequency precipitation radar to improve shallow precipitation detection in mountainous areas. *J. Appl. Meteor. Climatol.*, **62**, accepted.

Skofronick-Jackson, G., W. A. Petersen, W. Berg, C. Kidd, E. F. Stocker, D. B. Kirschbaum, R. Kakar, S. A. Braun, G. J. Huffman, T. Iguchi, P. E. Kirstetter, C. Kummerow, R. Meneghini, R. Oki, W. S. Olson, Y. N. Takayabu, K. Furukawa, and T. Wilheit, 2017: The Global Precipitation Measurement (GPM) mission for science and society. *Bull. Amer. Meteor. Soc.*, **98(8)**, 1679–1695.

Smith, P. L., 2016: Sampling issues in estimating radar variables from disdrometer data. *J. Atmos. Oceanic Technol.*, **33**, 2305–2313.

Smith, P. L., and Z. Liu, 1993: A study of sampling-variability effects in raindrop size observations. *J. Appl. Meteor.*, **32**, 1259–1269.

Speirs, P., M. Gabella, and A. Berne, 2017: A comparison between the GPM dual-frequency precipitation radar and ground-based radar precipitation rate estimates in the Swiss Alps and plateau. *J. Hydrometeor.*, **18**, 1247–1269.

Terao, T., F. Murata, M. Kiguchi, A. Fukushima, M. Tanoue, S. Ahmed, S. A. Choudhury, H. J. Syiemlieh, L. Cajee, A. K. Bhagabati, P. Bhattacharya, S. Dutta, R. Mahanta, and T. Hayashi, 2017: Direct validation of TRMM/PR near surface rain over the northeastern Indian subcontinent using a tipping bucket raingauge network. *SOLA*, **13**, 157–162.

Testud, J., S. Oury, R. A. Black, P. Amayenc, and X. Dou, 2001: The concept of ”normalized” distribution to describe raindrop spectra: a tool for cloud physics and cloud remote sensing. *J. Appl. Meteor.*, **40**, 1118–1140.

Tokay, A., L. P. D. Adderio, D. B. Wolff, and W. A. Petersen, 2020: Development and evaluation of the raindrop size distribution parameters for the nasa global precipitation measurement mission ground validation program. *J. Atmos. Oceanic Technol.*, **37**, 115–128.

Tokay, A., W. A. Petersen, P. Gatlin, and M. Wingo, 2013: Comparison of raindrop size distribution measurements by collocated disdrometers. *J. Atmos. Oceanic Technol.*, **30**, 1672–1690.

Tokay, A., D. B. Wolff, and W. A. Petersen, 2014: Evaluation of the new version of the laser-optical disdrometer, OTT Parsival^2. *J. Atmos. Oceanic Technol.*, **31**, 1276–1288.

Watters, D., A. Battaglia, K. Mroz, and F. Tridon, 2018: Validation of the GPM version-5 surface rainfall products over Great Britain and Ireland. *J. Hydrometeor.*, **19**, 1617–1636.

Willis, P. T., 1984: Functional fits to some observed drop size distributions and parameterization of rain. *J. Atmos. Sci.*, **41**, 1648–1661.

Wolff, D. B., and B. L. Fisher, 2008: Comparisons of instantaneous TRMM ground validation and satellite rain-rate estimates at different spatial scales. *J. Appl. Meteor. Climatol.*, **47**, 2215–2237.

Wolff, D. B., D. A. Marks, E. Amitai, D. S. Silberstein, B. L. Fisher, A. Tokay, J. Wang, and J. L. Pippitt, 2005: Ground validation for the Tropical Rainfall Measuring Mission (TRMM). *J. Atmos. Oceanic Technol.*, **22**, 365–380.

Yamaji, M., H. G. Takahashi, T. Kubota, R. Oki, A. Hamada, and Y. N. Takayabu, 2020: 4-year climatology of global drop size distribution and its seasonal variability observed by spaceborne dual-frequency precipitation radar. *J. Meteor. Soc. Japan*, **98(4)**, 755–773.

Table 5

Table 6

Table 7

Table 8

List of Figures

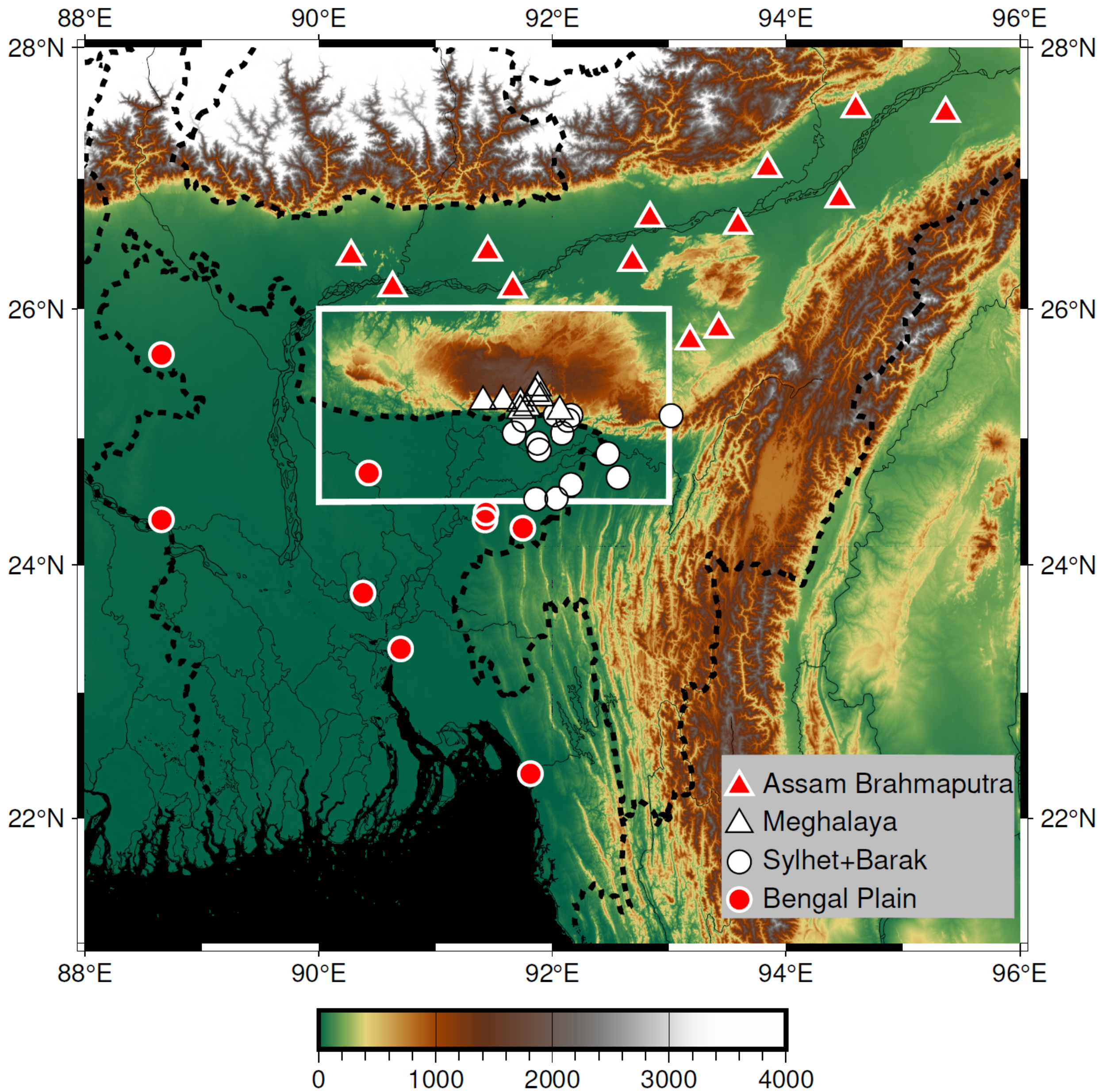

Fig. 1: Map of the northeastern Indian subcontinent. Rain gauges in four subregions: Assam Brahmaputra, Meghalaya, Sylhet+Barak, and Bengal Plain are indicated by red triangle, white triangle, white circle, and red circle, respectively. The topography was color-shaded (unit: m). A white rectangle corresponds to the region shown in Fig. 2.

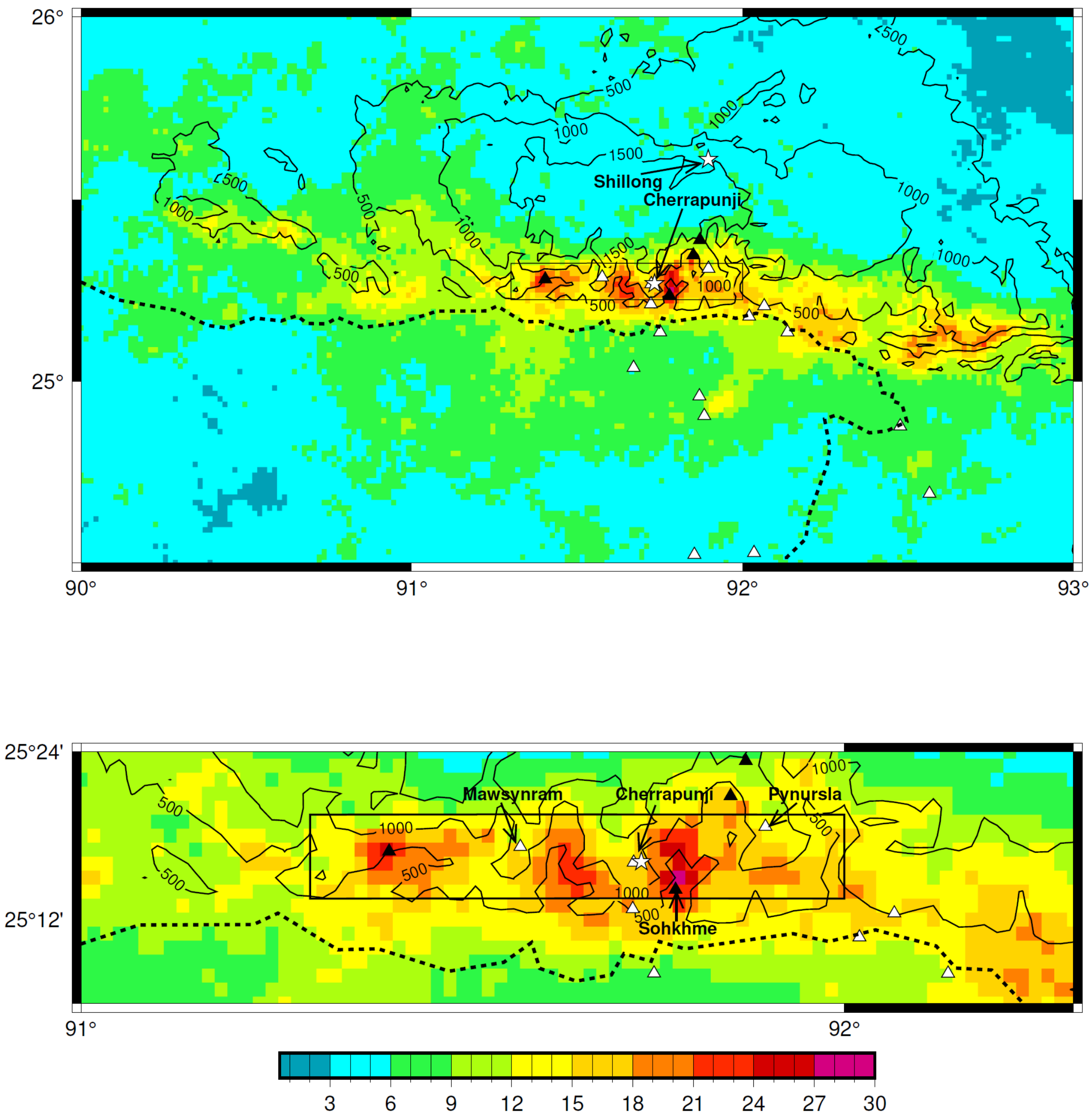

Fig. 2: (a) Rainfall distribution (shade, unit: mm day^{-1}) of TRMM PR climatology based on Hirose and Okada (2018) around the Meghalaya Plateau, and elevation (contour, unit: m). Open and closed triangles show the location of rain gauges installed before and after 2016, respectively. Star marks show the location of disdrometers. The black rectangle is the area defined as the heavy rainfall area (HRA). (b) Detail view around the HRA.

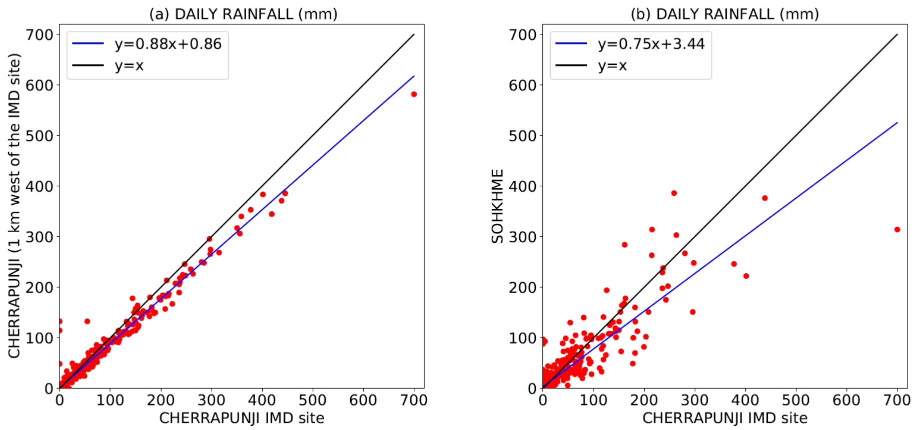

Fig. 3: Scatter plots of daily rainfalls (mm) between Cherrapunji IMD site on the horizontal axis and (a) Cherrapunji of our rain gauge network which is located around 1 km west of the IMD site, and (b) Sohkhme (see Fig. 2b) on the vertical axis. The black and blue solid lines are y=x, and regression line, respectively.

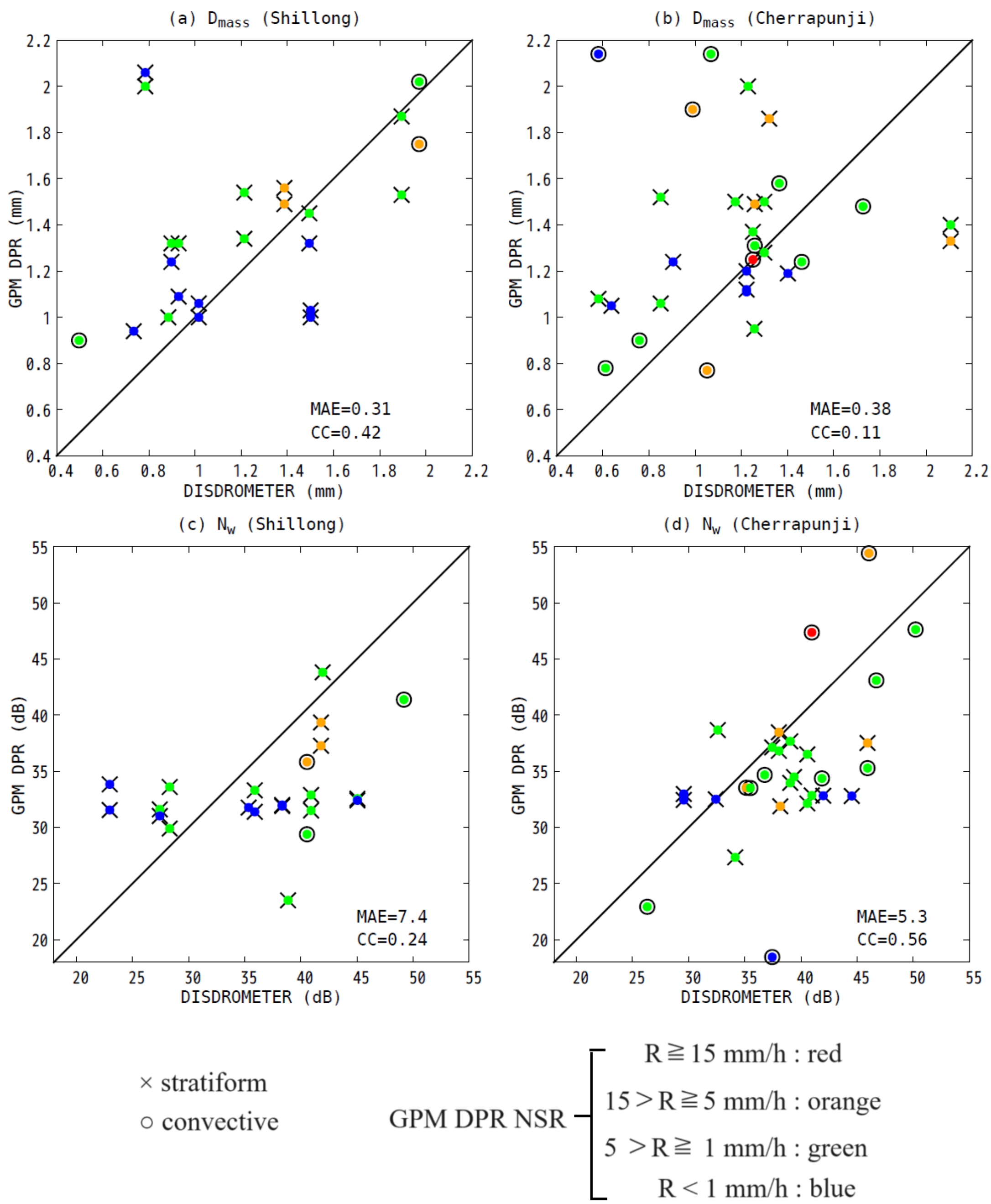

Fig. 4: Scatter plots of (a, b) D_{mass} and (c, d) N_{w} for a comparison between disdrometer and GPM DPR retrievals at (a, c) Shillong and (b, d) Cherrapunji. The black solid line shows the line y=x. Data from rainy cases for both disdrometers and GPM DPR products are plotted. Cross and circle marks represent stratiform and convective rains, respectively, based on the classification performed using the GPM DPR algorithm. Colors of the plots represent the GPM DPR NSR for (red) $R \geq 15$ mm h^{-1}, (orange) $15 > R \geq 5$ mm h^{-1}, (green) $5 > R \geq 1$ mm h^{-1}, and (blue) $R < 1$ mm h^{-1}, respectively. CC and MAE are correlation coefficient and mean absolute error, respectively.

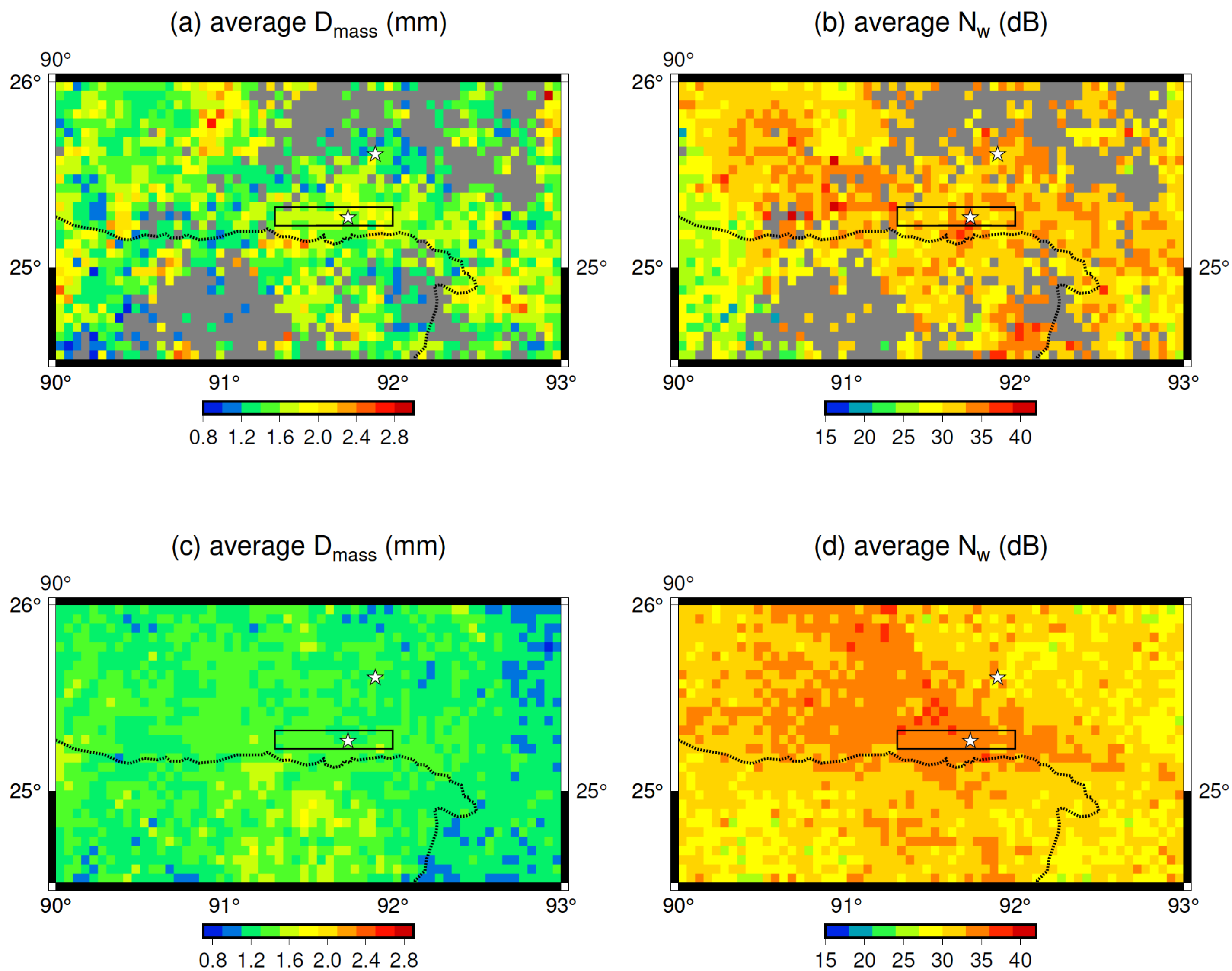

Fig. 5: (a, c) Average D_{mass} (mm) and (b, d) average N_{w} (dB) at the CFB level during the (a, b) premonsoon and (c, d) monsoon seasons. The grey color represents grids with an insufficient number of samples (less than 10 samples). The black rectangle and white stars represent the HRA and location of disdrometers, respectively.

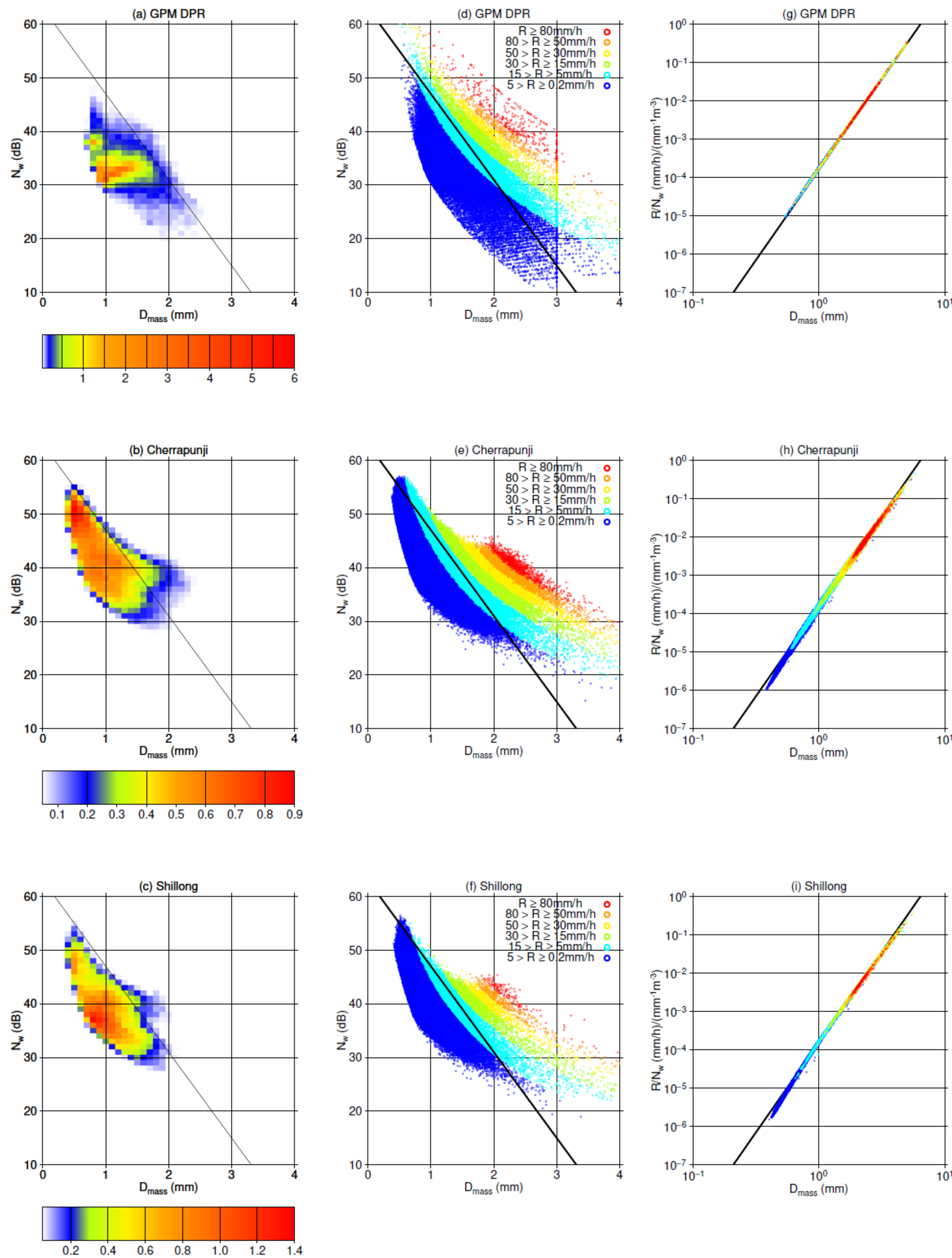

Fig. 6: (a–c) The density distribution (%) of D_{mass}–N_{w} diagrams. (d–f) The sample distribution of six rain rate categories in D_{mass}–N_{w} diagrams. (g–i) D_{mass}–N_{w}/R diagrams on a logarithmic axis. The colors of the samples are the same as (d–f). The data is (a, d, g) GPM DPR retrievals observed at the CFB level over the area (90°–93°E, 24.5°–26.0°N, see Fig. 2a). (b, e, h) Cherrapunji, and (c, f, i) Shillong, respectively. The solid line in (a–f) is the stratiform/convective separation line proposed by Bringi et al. (2009). Moreover, the solid line in (g–i) is the empirical equation derived from Liao et al. (2020).

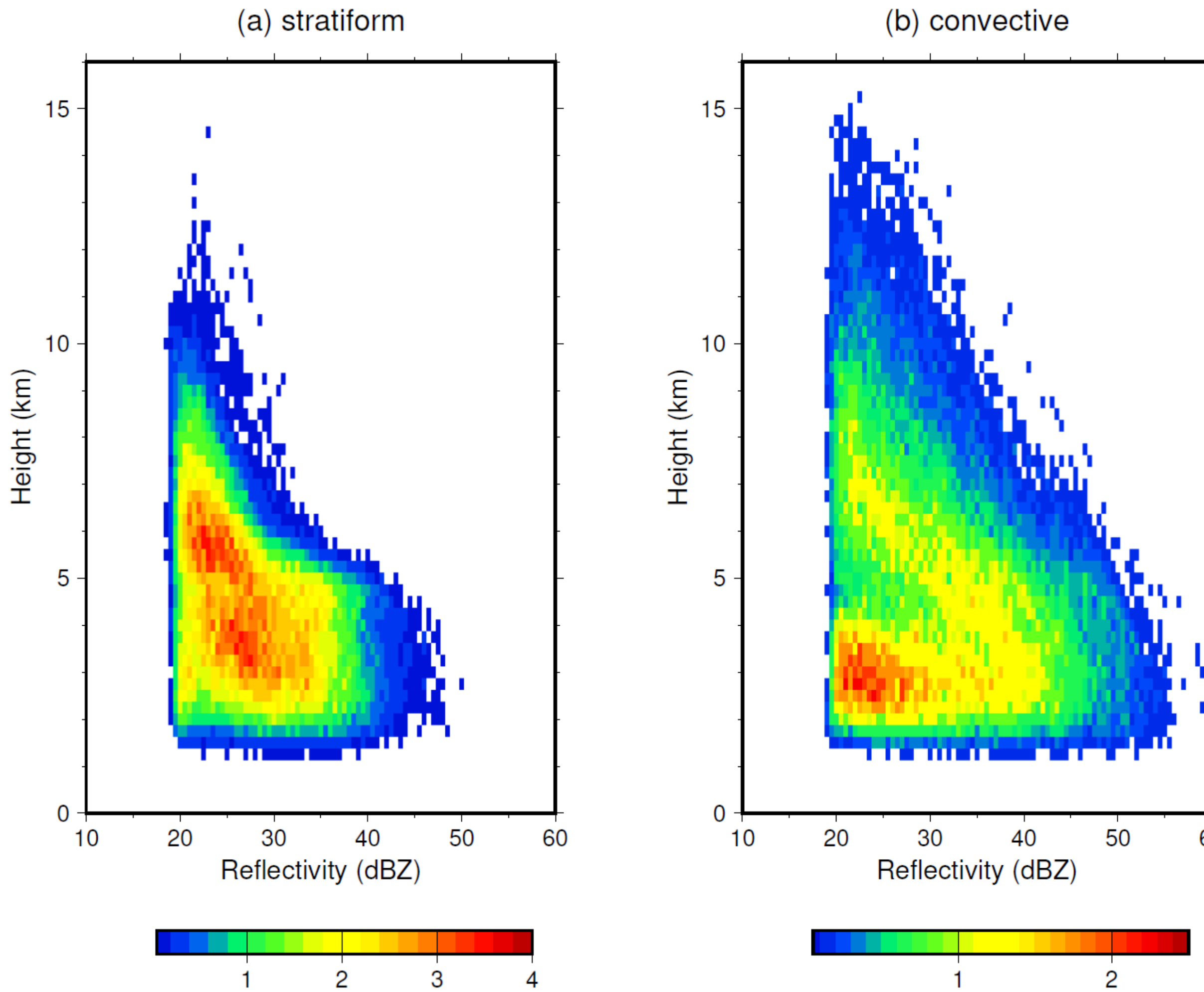

Fig. 7: CFADs (%) of (a) stratiform and (b) convective radar reflectivity within the HRA. The bin size in height is 0.25 km, and in reflectivity is 0.5 dBZ. The minimum of the shade is 0.05%.

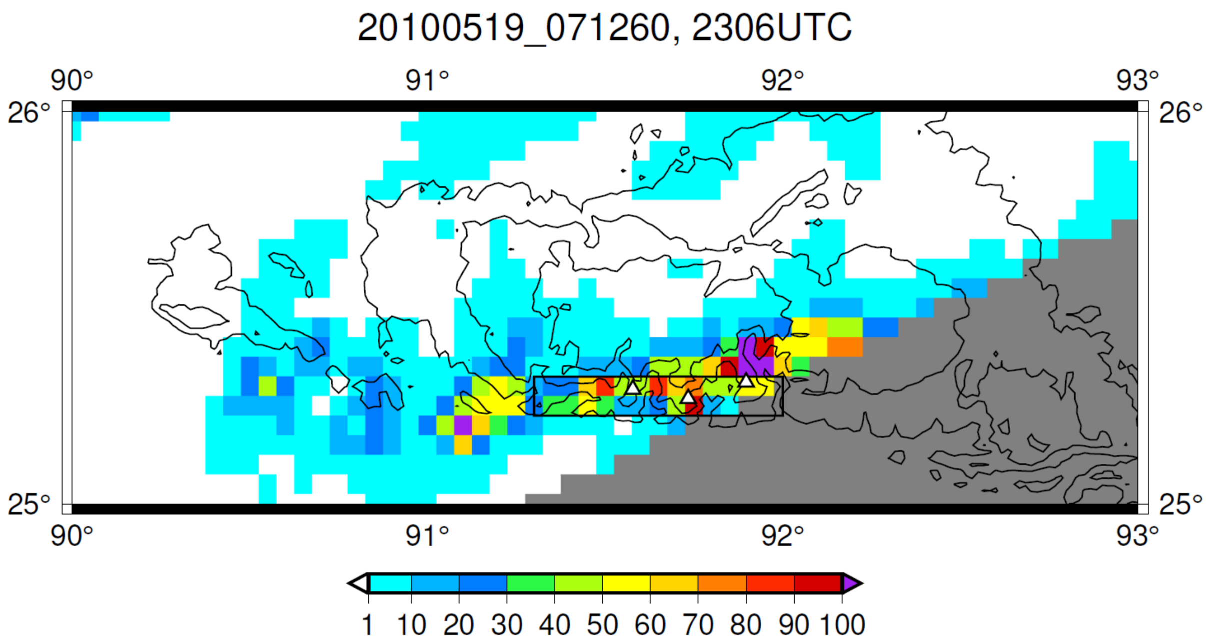

Fig. 8: NSR (unit: mm h^{-1}) distribution of the TRMM PR V8 path at 2306 UTC on 19th May 2010 for a rare heavy rainfall case, that intense rain rate of 156.0, 144.0, and 84.0 mm h^{-1} were observed at Mawsynram, Cherrapunji, and Pynursla stations, respectively (corresponding to the triangles aligned from west to east). The gray area was outside of the satellite path. Solid black lines are elevation contours at every 500 m interval.

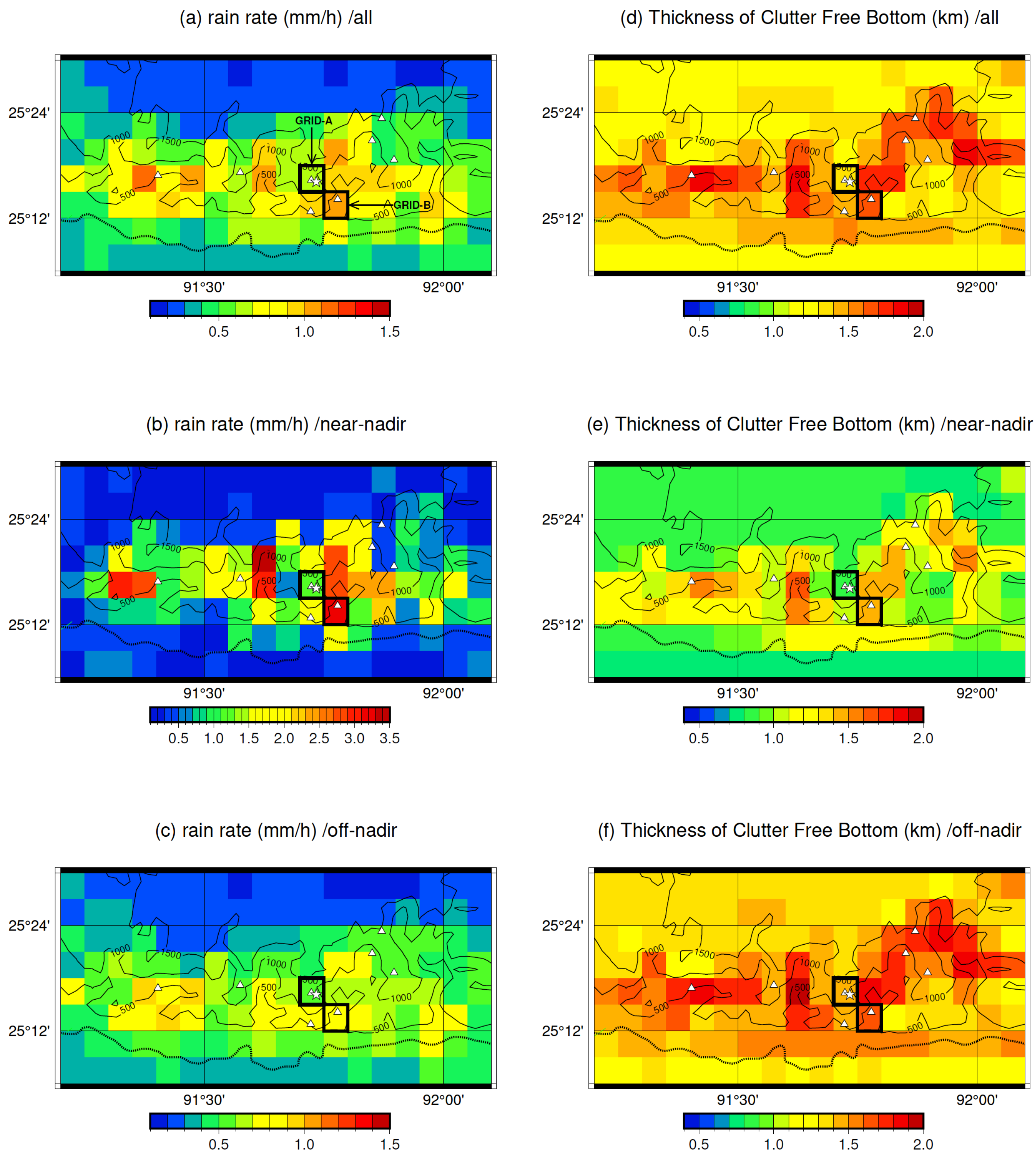

Fig. 9: (a–c) average NSR (mm h^{-1}) and (d–f) average thickness of CFB (m) for (a, d) all, (b, e) near-nadir, and (c, f) off-nadir bins in every 0.05°grid box. Solid black lines are elevation contours at every 500 m interval. The white triangles and stars are the location of rain gauges and disdrometers, respectively. Two bold rectangles where Cherrapunji and Sohkhme are located and labeled grid-A and grid-B, respectively, in Fig. 9a, which are used in Fig. 10.

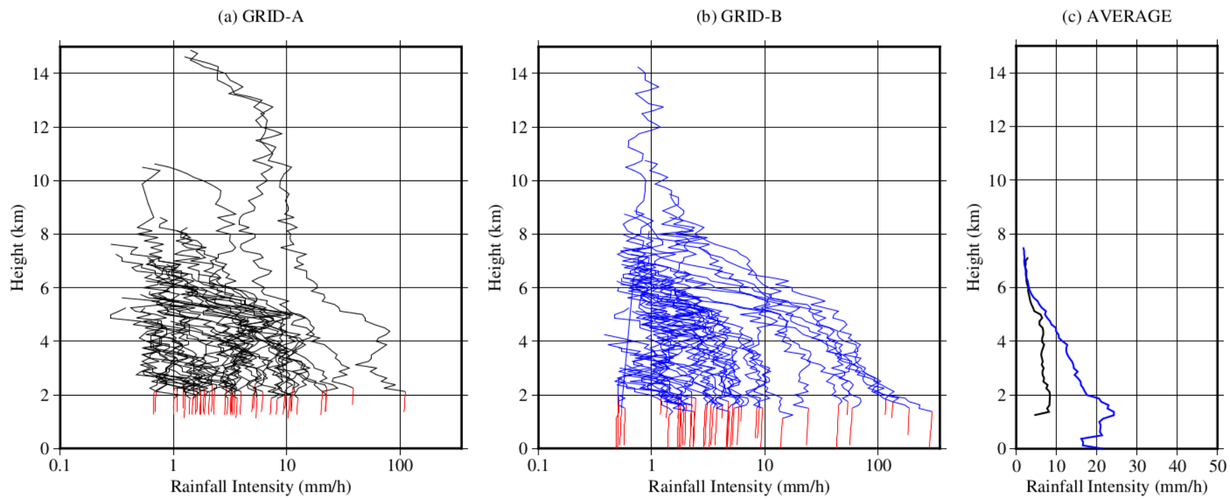

Fig. 10: Vertical profiles of rain rate for near-nadir bins within (a)grid-A and (b) grid-B. Red lines show the profiles between the CFB and the ground levels. (c)Average vertical profiles for grid-A (black) and grid-B (blue). The altitude at which the number of bins exceed 10 samples are averaged and displayed.

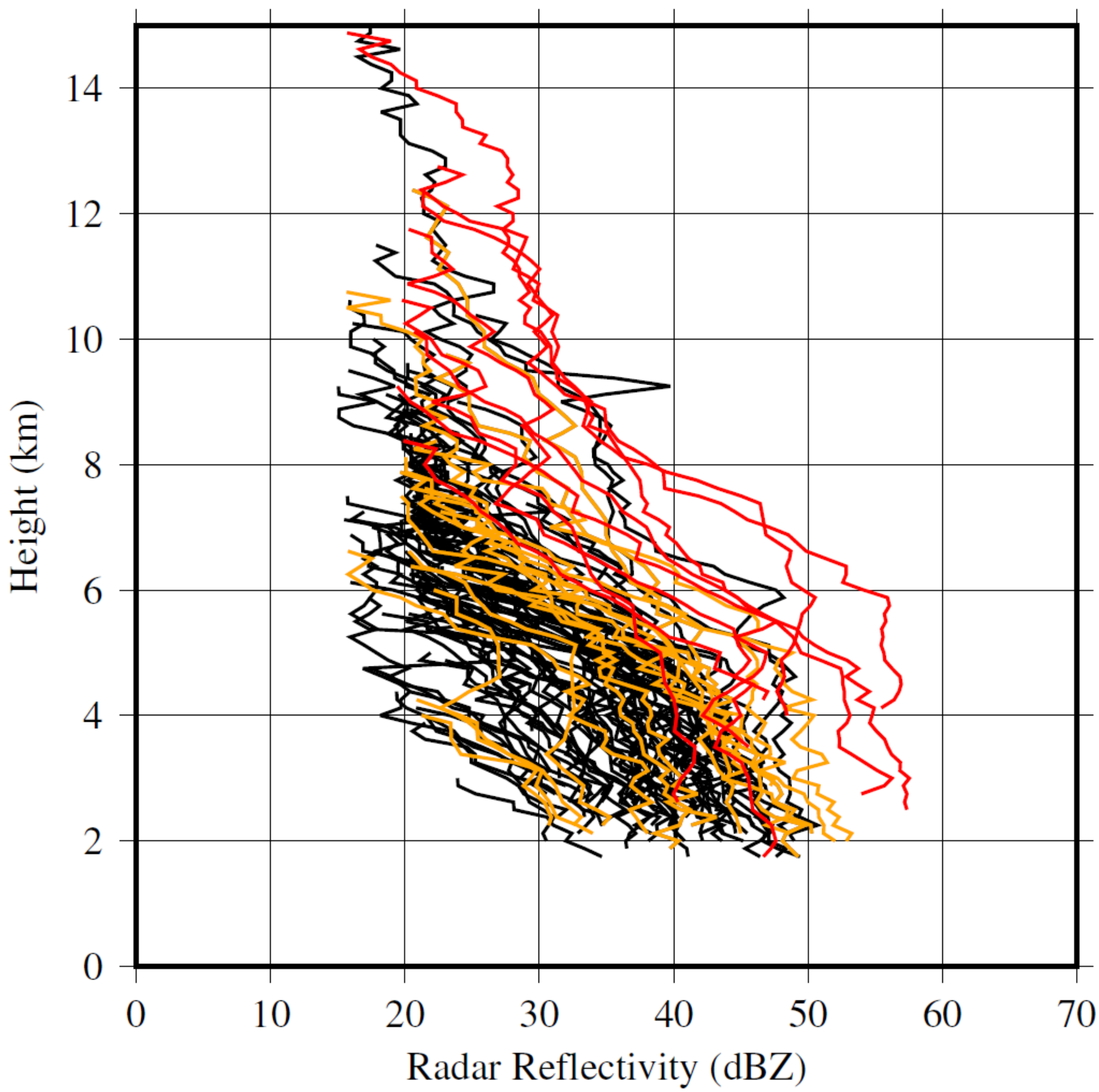

Fig. 11: Vertical profiles of reflectivity (dBZ) from spaceborne radars for heavy rainfall cases, that instant rain rate of rain gauges in the HRA excessed 30 mm h^{-1}. Red and orange lines denote cases with $\geq$ 80 mm h^{-1} and $\geq$ 60 mm h^{-1}, respectively.

List of Tables

Table 1: Validation of (a) TRMM PR V7, (b) TRMM PR V8, and (c) GPM DPR V6A with rain gauges, during the monsoon season (June–September). * and ** indicate significance at the 95% and 99% confidence levels, respectively. $\overline{RG}$ and $\overline{SAT}$ are the average rain rate of the matched rain gauge and NSR of satellites, respectively. $Bias = \frac{\overline{SAT}-\overline{RG}}{\overline{RG}}$. N_{obs} and N_{rain} are the total numbers of matchups and rainy samples of the satellites in N_{obs}, respectively.

(a) Area	$\overline{RG}$ (mm h^{-1})	$\overline{SAT}$ (mm h^{-1})	$\overline{SAT} - \overline{RG}$ (mm h^{-1})	$Bias$(%)	N_{obs}	N_{rain}
Meghalaya	2.24	1.18	-1.06	-47**	3849	725
Assam	0.43	0.36	-0.07	-16**	8422	878
Sylhet+Barak	1.03	0.70	-0.33	-32**	7445	1210
Bengal Plain	0.44	0.33	-0.11	-25**	6186	571
(b) Area	$\overline{RG}$ (mm h^{-1})	$\overline{SAT}$ (mm h^{-1})	$\overline{SAT}$-$\overline{RG}$ (mm h^{-1})	$Bias$(%)	N_{obs}	N_{rain}
Meghalaya	2.25	1.48	-0.77	-34**	3829	725
Assam	0.42	0.34	-0.08	-20**	8415	930
Sylhet+Barak	1.04	0.73	-0.32	-30**	7444	1262
Bengal Plain	0.45	0.30	-0.15	-34**	6149	595
(c) Area	$\overline{RG}$ (mm h^{-1})	$\overline{SAT}$ (mm h^{-1})	$\overline{SAT} - \overline{RG}$ (mm h^{-1})	$Bias$(%)	N_{obs}	N_{rain}
Meghalaya	2.17	1.23	-0.93	-43**	1177	275
Meghalaya/new	0.93	1.13	0.20	+21	507	84
Assam	0.46	0.35	-0.11	-24	2893	333
Sylhet+Barak	0.92	0.75	-0.17	-19	1715	296
Bengal Plain	0.43	0.58	0.15	+36	1134	126

Table 2: Validation of (a) TRMM PR V7, (b) TRMM PR V8, and (c) GPM DPR V6A with rain gauges. Same as Table 1 except for the premonsoon season (March–May).

(a) Area	$\overline{RG}$ (mm h^{-1})	$\overline{SAT}$ (mm h^{-1})	$\overline{SAT} - \overline{RG}$ (mm h^{-1})	$Bias(\%)$	N_{obs}	N_{rain}
Meghalaya	0.77	0.70	-0.07	-9	2725	221
Assam	0.16	0.23	+0.07	+45**	5652	318
Sylhet+Barak	0.28	0.34	+0.06	+23	5419	370
Bengal Plain	0.14	0.15	+0.01	+12*	4676	151
(b) Area	$\overline{RG}$ (mm h^{-1})	$\overline{SAT}$ (mm h^{-1})	$\overline{SAT} - \overline{RG}$ (mm h^{-1})	$Bias(\%)$	N_{obs}	N_{rain}
Meghalaya	0.80	0.66	-0.14	-18	2752	223
Assam	0.16	0.16	+0.00	+1	5678	330
Sylhet+Barak	0.27	0.24	-0.03	-11	5454	405
Bengal Plain	0.14	0.10	-0.04	-30	4675	172
(c) Area	$\overline{RG}$ (mm h^{-1})	$\overline{SAT}$ (mm h^{-1})	$\overline{SAT} - \overline{RG}$ (mm h^{-1})	$Bias(\%)$	N_{obs}	N_{rain}
Meghalaya	0.84	0.64	-0.20	-24	908	75
Meghalaya/new	0.29	0.17	-0.12	-43	393	27
Assam	0.20	0.17	-0.03	-15	2162	172
Sylhet+Barak	0.27	0.26	-0.02	-6	1259	94
Bengal Plain	0.43	0.17	-0.26	-60	854	42

Table 3: Number of rain and no rain events observed at (a–c) Cherrapunji and (d–f) Shillong by the disdrometer and the GPM DPR for (a,d) all periods, (b,e) the monsoon season, and (c,f) the premonsoon season.

(a) Cherrapunji: all

sum		disdrometer	
360		rain	no rain
DPR	rain	30	7
	no rain	27	296

(b) Cherrapunji: monsoon

sum		disdrometer	
130		rain	no rain
DPR	rain	23	6
	no rain	19	82

(c) Cherrapunji: premonsoon

sum		disdrometer	
72		rain	no rain
DPR	rain	3	0
	no rain	4	65

(d) Shillong: all

sum		disdrometer	
291		rain	no rain
DPR	rain	23	6
	no rain	8	254

(e) Shillong: monsoon

sum		disdrometer	
99		rain	no rain
DPR	rain	9	4
	no rain	8	78

(f) Shillong: premonsoon

sum		disdrometer	
67		rain	no rain
DPR	rain	10	1
	no rain	0	56

Table 4: Contingency tables of rainfall at rain gauges in the HRA and the matchups of the TRMM PR and GPM DPR for (a) near-nadir and (b) off-nadir data.

(a) near-nadir

sum		rain gauges	
1305		rain	no rain
radars	rain	96	62
	no rain	16	1131

(b) off-nadir

sum		rain gauges	
7603		rain	no rain
radars	rain	333	381
	no rain	175	6714

Supplement 1: List of raingauge stations used for the validation with TRMM PR (Meghalaya & Assam)

Area Name	Station Name	Longitude	Latitude	Periods	Num. samples
Meghalaya	Amlarem	92.1202	25.2943	April 11, 2006 – August 05, 2008	744
Meghalaya	Cherrapunji	91.7239	25.2723	April 19, 2006 – October 06, 2014	1918
Meghalaya	Mawsynram	91.5755	25.2869	May 23, 2006 – October 06, 2014	2405
Meghalaya	Nongtalang	92.0654	25.2077	June 20, 2009 – February 25, 2014	1167
Meghalaya	Pynursla	91.8966	25.3109	June 18, 2006 – February 25, 2014	2087
Meghalaya	Thangkharang Park1	91.7237	25.2172	November 16, 2006 – September 30, 2008	596
Meghalaya	Thangkharang Park2	91.7227	25.2128	February 21, 2009 – October 06, 2014	1580
Meghalaya/ new	Mawjngh	91.8709	25.3892	-	0
Meghalaya/ new	Nongkenbah	91.4035	25.2814	-	0
Meghalaya/ new	Sohkhme	91.7789	25.2358	-	0
Meghalaya/ new	Wahkhen	91.8510	25.3474	-	0
Assam	Bokakhat	93.5891	26.6409	March 07, 2013 – September 01, 2014	519
Assam	Diphu	93.4248	25.8426	July 02, 2006 –October 07, 2014	866
Assam	Goalpara	90.6306	26.1612	June 26, 2006 – March 03, 2012	1534
Assam	Guwahati	91.6579	26.1526	March 18, 2006 – October 03, 2014	2833
Assam	Kokrajhar	90.2762	26.4044	March 07, 2008 – October 05, 2014	1561
Assam	Lumding	93.1781	25.7513	July 02, 2006 – October 07, 2014	1420
Assam	Moridhal	94.5958	27.5331	July 08, 2006 – October 05, 2014	2498
Assam	Nagaon	92.6858	26.3571	May 27, 2006 – October 07, 2014	2086
Assam	Nalbari	91.4439	26.4365	July 20, 2006 – October 07, 2014	1940
Assam	Sankardev College	93.8404	27.0768	July 09, 2006 – October 07, 2014	2460
Assam	Teok	94.4581	26.8447	March 04, 2008 – October 07, 2014	1506
Assam	Tezpur	92.8372	26.6973	May 27, 2006 – October 07, 2014	2587
Assam	Tinskia	95.3644	27.4980	February 20, 2007 – October 04, 2014	2116

Supplement 2: List of raingauge stations used for the validation with TRMM PR (Sylhet+Barak & Bengal Plain)

Area Name	Station Name	Longitude	Latitude	Periods	Num. samples
Sylhet+Barak	Amarshid	92.4764	24.8768	March 10, 2006 – October 06, 2014	2352
Sylhet+Barak	Bulaganj	91.7506	25.1361	May 12, 2006 – October 06, 2014	2595
Sylhet+Barak	Chhatak	91.6704	25.0379	March 10, 2006 – October 06, 2014	2676
Sylhet+Barak	Haflong	93.0181	25.1723	August 09, 2006 – October 06, 2014	788
Sylhet+Barak	Hailakandi	92.5651	24.6908	August 09, 2006 – October 06, 2014	1261
Sylhet+Barak	Jaflong	92.0198	25.1791	March 08, 2007 – October 06, 2014	2206
Sylhet+Barak	BARI, Jaintapur	92.1359	25.1359	May 11, 2006 – October 06, 2014	2362
Sylhet+Barak	Juri	92.1617	24.6361	March 13, 2006 – March 04, 2007	295
Sylhet+Barak	Kulaura	92.0345	24.5270	March 08, 2007 – October 06, 2014	2041
Sylhet+Barak	Naljuri	92.1617	25.1751	May 11, 2006 – March 02, 2007	252
Sylhet+Barak	Rajnagar	91.8542	24.5222	May 11, 2006 – October 06, 2014	2621
Sylhet+Barak	Sylhet	91.8842	24.9055	May 11, 2006 – October 06, 2014	2157
Sylhet+Barak	Sylhet Airport	91.8694	24.9595	March 11, 2007 – October 06, 2014	2182
Bengal Plain	Chittagong	91.8085	22.3531	August 07, 2004 – October 03, 2014	2903
Bengal Plain	Dhaka	90.3784	23.7799	August 15, 2004 – October 06, 2014	2900
Bengal Plain	Dinajpur	88.6545	25.6466	March 06, 2005 – March 05, 2014	2680
Bengal Plain	BRRI, Habiganj	91.4286	24.4149	March 08, 2007 – October 06, 2014	1704
Bengal Plain	Mymensingh	90.4263	24.7256	August 04 2004 – September 12, 2014	3175
Bengal Plain	Rajshahi	88.6549	24.3606	August 11, 2004 – March 08, 2014	2899
Bengal Plain	Srimangal	91.7438	24.2950	March 08, 2007 – October 06, 2014	2031

Supplement 3: List of raingauge stations used for the validation with GPM DPR (Meghalaya & Assam)

Area Name	Station Name	Longitude	Latitude	Periods	Num. samples
Meghalaya	Amlarem	92.1202	25.2943	-	0
Meghalaya	Cherrapunji	91.7239	25.2723	May 03, 2014 – July 31, 2019	705
Meghalaya	Mawsynram	91.5755	25.2869	March 09, 2014 – March 05, 2020	825
Meghalaya	Nongtalang	92.0654	25.2077	October 26, 2014 – March 05, 2020	720
Meghalaya	Pynursla	91.8966	25.3109	October 26, 2014 – March 02, 2020	716
Meghalaya	Thangkharang Park1	91.7237	25.2172	-	0
Meghalaya	Thangkharang Park2	91.7227	25.2128	March 09, 2014 – March 05, 2020	690
Meghalaya/ new	Mawjngh	91.8709	25.3892	April 20, 2016 – July 02, 2018	288
Meghalaya/ new	Nongkenbah	91.4035	25.2814	January 02, 2016 – March 11, 2019	433
Meghalaya/ new	Sohkhme	91.7789	25.2358	March 16, 2016 – March 03 2019,	395
Meghalaya/ new	Wahkhen	91.8510	25.3474	March 06, 2017 – March 02, 2020,	419
Assam	Bokakhat	93.5891	26.6409	March 19, 2014 – March 01, 2019,	616
Assam	Diphu	93.4248	25.8426	March 19, 2014 – February 23, 2020,	800
Assam	Goalpara	90.6306	26.1612	February 17, 2015 – March 03, 2020,	411
Assam	Guwahati	91.6579	26.1526	March 09, 2014 – March 05, 2020,	810
Assam	Kokrajhar	90.2762	26.4044	March 09, 2014 – February 18, 2019	665
Assam	Lumding	93.1781	25.7513	March 19, 2014 – February 20, 2020	826
Assam	Moridhal	94.5958	27.5331	March 19, 2014 – March 02, 2020	832
Assam	Nagaon	92.6858	26.3571	March 09, 2014 – February 23, 2020	812
Assam	Nalbari	91.4439	26.4365	March 09, 2014 – February 18, 2019	672
Assam	Sankardev College	93.8404	27.0768	March 19, 2014 – March 02, 2020	846
Assam	Teok	94.4581	26.8447	March 19, 2014 – February 26, 2019	707
Assam	Tezpur	92.8372	26.6973	March 09, 2014 – March 05, 2020	786
Assam	Tinskia	95.3644	27.4980	March 09, 2014 – February 26, 2019	621

Supplement 4: List of raingauge stations used for the validation with GPM DPR (Sylhet+Barak & Bengal Plain)

Area Name	Station Name	Longitude	Latitude	Periods	Num. samples
Sylhet+Barak	Amarshid	92.4764	24.8768	March 22, 2014 – March 03, 2019	717
Sylhet+Barak	Bulaganj	91.7506	25.1361	March 09, 2014 – March 05, 2020	787
Sylhet+Barak	Chhatak	91.6704	25.0379	March 09, 2014 – March 09, 2019	665
Sylhet+Barak	Haflong	93.0181	25.1723	May 25, 2014 – February 23, 2020	782
Sylhet+Barak	Hailakandi	92.5651	24.6908	May 24, 2014 – February 26, 2018	514
Sylhet+Barak	Jaflong	92.0198	25.1791	May 09, 2014 – March 05, 2020	762
Sylhet+Barak	BARI, Jaintapur	92.1359	25.1359	March 09, 2014 – March 05, 2020	460
Sylhet+Barak	Juri	92.1617	24.6361	-	0
Sylhet+Barak	Kulaura	92.0345	24.5270	March 22, 2014 – March 10, 2015	132
Sylhet+Barak	Naljuri	92.1617	25.1751	-	0
Sylhet+Barak	Rajnagar	91.8542	24.5222	March 09, 2014 – March 03, 2019	672
Sylhet+Barak	Sylhet	91.8842	24.9055	March 09, 2014 – August 11, 2019	249
Sylhet+Barak	Sylhet Airport	91.8694	24.9595	March 09, 2014 – March 03, 2019	184
Bengal Plain	Chittagong	91.8085	22.3531	March 29, 2014 – March 07, 2015	121
Bengal Plain	Dhaka	90.3784	23.7799	March 09, 2014 – November 05, 2018	521
Bengal Plain	Dinajpur	88.6545	25.6466	August 11, 2015 – March 08, 2019	471
Bengal Plain	BRRI, Habiganj	91.4286	24.4149	March 09, 2014 – August 09, 2019	696
Bengal Plain	Mymensingh	90.4263	24.7256	March 09, 2014 – September 10, 2018	539
Bengal Plain	Rajshahi	88.6549	24.3606	August 11, 2015 – March 08, 2019	471
Bengal Plain	Srimangal	91.7438	24.2950	March 09, 2014 – July 29, 2018	582